# Regional Characteristics of Observable Foreshocks

Nadav Wetzler\*<sup>1</sup>, Emily E. Brodsky<sup>2</sup>, Esteban J. Chaves<sup>3</sup>, Thomas Goebel<sup>4</sup>, and Thorne Lay<sup>2</sup>

#### **Abstract**

Measures of foreshock occurrence are systematically examined using earthquake catalogs for eight regions (Italy, southern California, northern California, Costa Rica, Onshore Japan, Alaska, Turkey, and Greece) after imposing a magnitude ≥ 3.0 completeness level. Foreshocks are identified using three approaches: a magnitude-dependent space + fixed-time windowing method, a nearest-neighbor clustering method, and a modified magnitude-dependent space + variable-time windowing method. The method with fixed-time windows systematically yields higher counts of foreshocks than the other two clustering methods. We find similar counts of foreshocks across the three methods when the magnitude aperture is equalized by including only earthquakes in the magnitude range  $M^*-2 \le M < M^*$ , in which  $M^*$  is the mainshock magnitude. For most of the catalogs (excluding Italy and southern California), the measured b-values of the foreshocks of all region-specific mainshocks are lower by 0.1-0.2 than b-values of respective aftershocks. Allowing for variable-time windows results in relatively high probabilities of having at least one foreshock in Italy (~43%-56%), compared to other regional catalogs. Foreshock probabilities decrease to 14%-41% for regions such as Turkey, Greece, and Costa Rica. Similar trends are found when requiring at least five foreshocks in a sequence to be considered. Estimates of foreshock probabilities for each mainshock are method dependent; however, consistent regional trends exist regardless of method, with regions such as Italy and southern California producing more observable foreshocks than Turkey and Greece. Some regions with relatively high background seismicity have comparatively low probabilities of detectable foreshock activity when using methods that account for variable background, possibly due to depletion of near-failure fault conditions by background activity.

Cite this article as Wetzler, N., E. E. Brodsky, E. J. Chaves, T. Goebel, and T. Lay (2022). Regional Characteristics of Observable Foreshocks, *Seismol. Res. Lett.* 94, 428–442, doi: 10.1785/0220220122.

**Supplemental Material** 

#### Introduction

Aftershock productivity is to first order a function of mainshock magnitude and can usually be well described by a power law or an exponential relationship for mainshock sequences (e.g., Utsu, 1970; Ogata, 1988; Reasenberg and Jones, 1989; Utsu et al., 1995; Helmstetter et al., 2003; Felzer et al., 2004). However, the detection of foreshock activity is generally more ambiguous and complex, being strongly dependent on the seismic network resolution as well as the mainshock magnitude relative to the completeness level of the catalog (Mignan, 2014; Trugman and Ross, 2019; van den Ende and Ampuero, 2020). Observed variations in aftershock productivity levels have been attributed to influence of the regional tectonic setting (Singh and Suárez, 1988; Wetzler et al., 2016; Dascher-Cousineau et al., 2020), the occurrence of foreshocks (Marsan et al., 2014), and the mainshock source properties (Persh and Houston, 2004; Tahir and Grasso, 2015; Wetzler et al., 2016). In addition, aftershock distribution and faulting style are affected by mechanical conditions and transient stress changes at the periphery of the mainshock (Hasegawa *et al.*, 2012; Wetzler *et al.*, 2017, 2018). Foreshocks may also be affected by differences in crustal conditions if both foreshocks and aftershocks are a result of the same triggering processes (Helmstetter and Sornette, 2003).

Recent studies in California and Japan have provided a broad range of possible foreshock rates and thus have reopened the debate on the frequency of foreshock occurrence. For instance, Tamaribuchi *et al.* (2018) demonstrated that foreshock sequences (including two or more events) in the Japan Meteorology Agency catalog occur for 30%–40% of the identified mainshocks. In California, the recent observations have

<sup>1.</sup> Geological Survey of Israel, Jerusalem, Israel, https://orcid.org/0000-0002-7552-0866 (NW); 2. Department of Earth and Planetary Sciences, University of California Santa Cruz, Santa Cruz, California, U.S.A., https://orcid.org/0000-0002-6855-6860 (EEB); https://orcid.org/0000-0003-2360-4213 (TL); 3. Volcanological and Seismological Observatory of Costa Rica at Universidad Nacional (OVSICORI-UNA), Heredia, Costa Rica, https://orcid.org/0000-0002-5724-1513 (EJC); 4. Center for Earthquake Research and Information, University of Memphis, Memphis, U.S.A.

<sup>\*</sup>Corresponding author: nadavw@gsi.gov.il

<sup>©</sup> Seismological Society of America

suggested that the probability of detecting at least one foreshock relative to a Poisson distribution of background rate over a one-year interval prior to a mainshock is ~72% when using a catalog with a low magnitude of completeness achieved by advanced waveform processing for a high-resolution seismic network (e.g., Trugman and Ross, 2019). However, this estimate has been contested by van den Ende and Ampuero (2020) who find that the probability for foreshocks is ~18%-33%, comparable to that in Japan, when considering non-Poissonian and temporally fluctuating background seismicity. Further examination of the elevated foreshock activity recognized by Trugman and Ross (2019) suggested that 20% of the mainshocks preceded by increased seismicity rate cannot be represented by the epidemic type aftershock sequence (ETAS) models (Moutote et al., 2021). Variations in foreshock occurrence are also observed when considering the faulting style of the mainshock with strike-slip faulting in California having higher tendency for foreshocks than reverse or normal faulting (Chen and Shearer, 2016).

At the global scale, foreshocks tend to share the same faulting style as the mainshock (e.g., Wetzler *et al.*, 2017), in some cases exhibiting a precursory migration toward the mainshock hypocenter, as observed prior to the occurrence of the 2011  $M_{\rm w}$  9.2 Tohoku, Japan, and the 2014  $M_{\rm w}$  8.2 Iquique, Chile, earthquakes (e.g., Kato and Igarashi, 2012; Brodsky and Lay, 2014; Ruiz *et al.*, 2014). Global earthquake catalogs, which have a relatively high magnitude of completeness, indicate that for interplate thrust faulting mainshocks foreshocks are more commonly detected than for other mainshock faulting geometries (Reasenberg, 1999), opposite to the reported regional behavior in California.

Here, foreshock occurrence at regional scales is studied using eight seismicity catalogs with varying tectonic settings and magnitude of completeness. We use the highest regional completeness level ( $M_{\rm c}$  3.0) across all regions to allow for a uniform analysis. Established procedures and a modified classic procedure are applied to identify earthquake clusters and count foreshocks. Sequences are classified from conventional mainshocks to multiplets and/or swarms using the magnitude differences between the largest events and their strongest foreshocks or aftershocks. The effects of the clustering method on the estimated foreshock occurrence and the regional variations are considered.

#### **Dataset**

Earthquake sequences are defined by clustering procedures for shallow depth ( $\leq$ 70 km) events using eight independent seismicity catalogs (Fig. 1): (1) Inland Italy from 1995 to 2020, (2) southern California from 1985 to 2020, (3) northern California from 1995 to 2022, (4) Costa Rica from 2010 to 2021, (5) Inland Japan from 1990 to 2011 prior to the Tohoku  $M_{\rm w}$  9.1 event, (6) Alaska–Aleutians from 2010 to 2021, (7) Turkey from 1995 to 2021, and (8) Greece from 2012 to 2022 (see Data and Resources, for specific origin of each catalog).

To provide comparable seismicity sampling between the regions for foreshock counting, we search for the maximum magnitude of completeness  $(M_c)$  among the regional values of  $M_c$  for the eight catalogs. The magnitude of completeness,  $M_c$ , is computed iteratively from the goodness of fit using a Kolmogorov-Smirnov test with a smoothing constraint between observed and theoretical Gutenberg-Richter distributions with b-values from maximum-likelihood estimation (e.g., Goebel et al., 2017).  $M_c$  varies from 2.4 to 2.9 for the regional catalogs (Fig. S1, available in the supplemental material to this article). We next use a uniform  $M_c$  of 3.0 for all the eight catalogs, representing a +0.1 magnitude level above the largest regional  $M_c$  (Turkey, 2.9, Fig. S1). The maximum-likelihood b-values for the complete catalogs with  $M_c$  3.0 are found to be 0.9 for Italy, Greece, southern California, and Turkey, whereas b-values decrease to 0.7 and 0.8 for the subduction zones in Japan and Costa Rica, respectively. The estimated statistical uncertainty of each b-value,  $\sigma_b$ , ranges from 0.003 to 0.007 (Shi and Bolt, 1982), but we give b-value estimates to only one decimal point precision. The relationship by Shi and Bolt provides an estimate of the statistical uncertainty in the exponent that does not consider overall data misfit or contribution from uncertainty in  $M_c$  estimates. All eight catalogs show increasing departures from a constant b-value slope about 1.5-2 magnitude units above  $M_c$ , favoring maximumlikelihood estimation of b-value over the standard least-squares regression, which would otherwise indicate higher slopes from  $M_c$  to the largest catalog magnitudes. This under-sampling of large events is the expected result of having variable time intervals of 1-3.5 decades for each catalog that do not capture the full seismic cycle of the region. The zero-magnitude intercepts (a-values) range from 6.0 to 7.3, reflecting the varying scale and activity level above completeness of each region.

#### **Earthquake Clusters**

For each catalog, we distinguish earthquake clusters from background activity based on temporal and spatial criteria, defining foreshock and aftershock sequences associated with the largest magnitude event in each cluster. Given the intrinsic uncertainty in separating out the background and the potential dependency of the measurements on the specific clustering method (Mizrahi *et al.*, 2021), three independent methods are used to cluster the activity.

### Magnitude-varying space + fixed-time windowing —"WnC"

Earthquake sequences are usually quite concentrated in space and time, and many foreshock and aftershock analyses isolate the clustered events by capturing all events in space–time windows defined by different criteria (e.g., Jones and Molnar, 1976; Chen and Shearer, 2016; Dascher-Cousineau *et al.*, 2020). We first associate earthquakes with clusters for each identified mainshock using a magnitude-dependent spatial window with

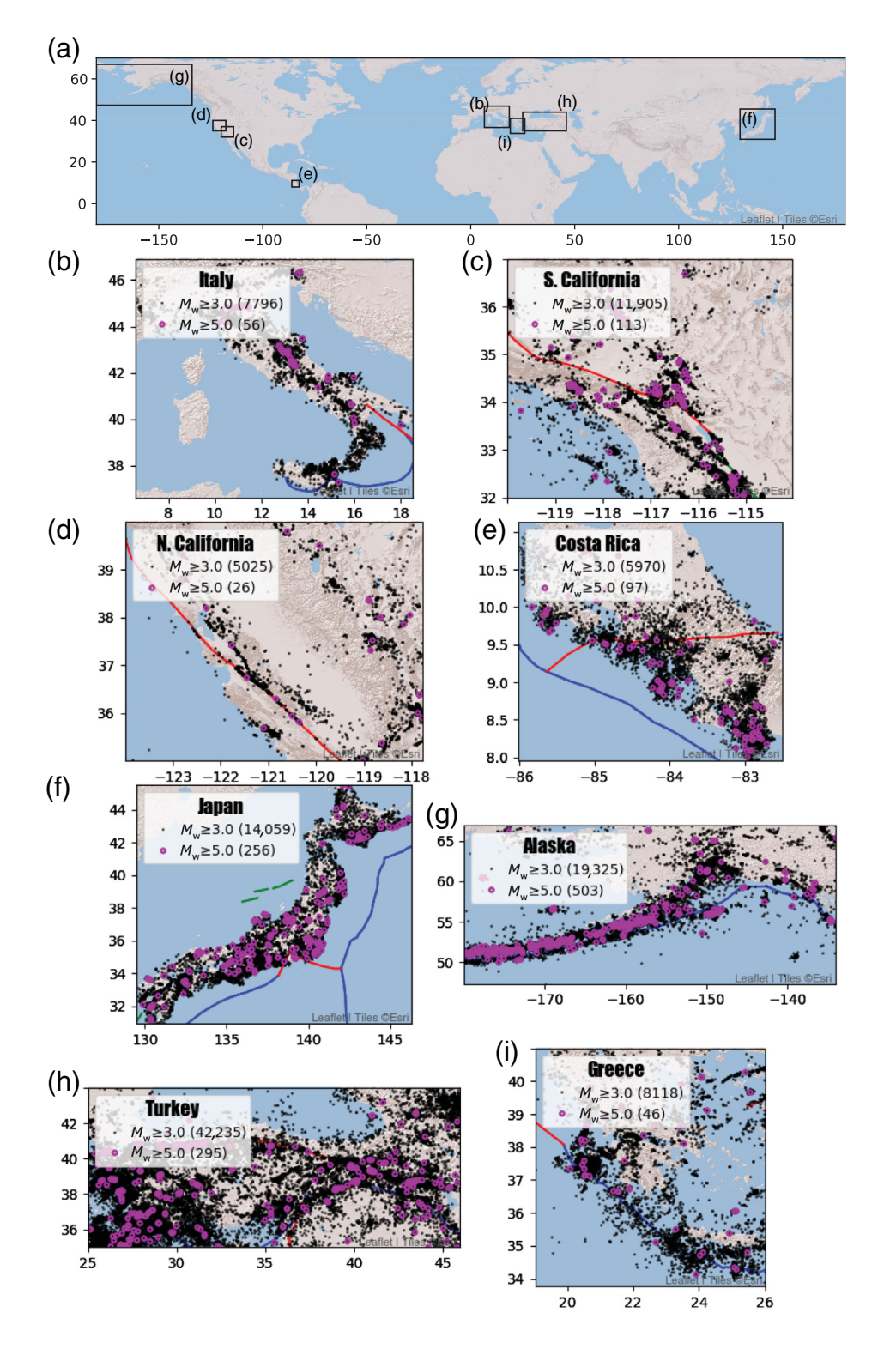


**Figure 1.** Seismicity maps for all earthquakes above the unified completeness level ( $M_c$  3.0) for each of the eight catalogs considered in this study (a), with the largest magnitude earthquakes ( $M_w \ge 5.0$ ) highlighted by the magenta circles. The number of earthquakes for each magnitude cutoff are presented in the legend. (b) Inland Italy activity spans from 1995 to 2020, (c) southern California from 1985 to 2020, (d) northern California from 1995 to 2022, (e) Costa Rica from 2010 to 2021, (f) Inland Japan from 1990 to 2011 prior to the Tohoku  $M_w$  9.1 event, (g) Alaska–Aleutians from 2010 to 2021, (h) Turkey from 1995 to 2021, and (i) Greece from 2012 to 2022. See Data and Resources for specific origin of each catalog. Plate boundaries: transforms (red), trenches (blue), and ridges (green) are plotted following Bird (2003).

a fixed temporal window of 30 days prior the mainshock and 60 days after. Earthquaketo-cluster association initiates from the strongest magnitude event in each catalog and works downward. The spatial dimension of each cluster, R, is assigned by a radius from the mainshock hypocenter given by a scaled value of the magnitude-based mainshock rupture length  $(L_{WnC})$  estimated by Wells and Coppersmith (1994), adjusted to account for the long rupture lengths of some great megathrust earthquakes:

$$R = L_{WnC} \times q$$
  
 $q = \{ \text{if } M \ge 9; 1.5, \text{if } 9 \ge M > 8; 2.0,$   
 $\text{if } M \le 8; 1 \}.$  (1)

Using a 30-day window preceding and 60-day window following each mainshock (e.g., Felzer et al., 2004) is a sensible but arbitrary choice for uniformity of processing, given that the Omori-like decay of each sequence to background level presents great difficulties for defining the end of both large and small sequences. All events with  $M \ge 3.0$  within the space-time windows are then counted, without explicit adjustment for presence of any overlapping background activity. For regions with low background rates, little contamination of earthquake counts in the space-time windows is expected for our magnitude cutoff, but increasing contamination is likely for higher background rate regions. We abbreviate this method WnC for Wells Coppersmith. The likelihood of significant contamination for WnC clustering grows for lower completeness levels for

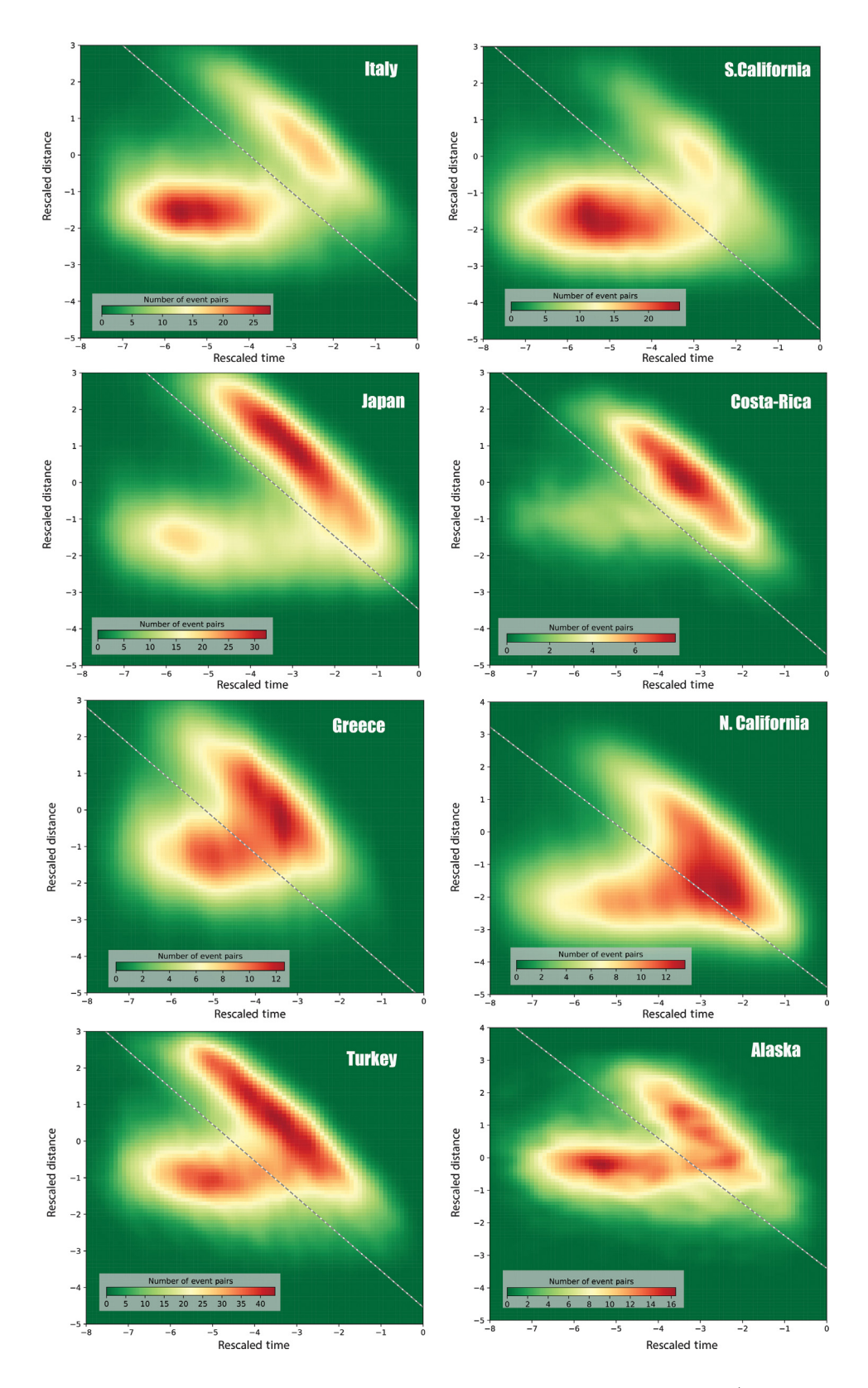


**Figure 2.** Cumulative distributions of the rescaled spatial and temporal  $(T_{ij} = t_{ij} 10^{-qbm_i})$  distances  $(R_{ij} = (r_{ij})^{d_f} 10^{-(1-q)bm_i})$  between event (i, j) pairs calculated for all events in the eight catalogs with earthquake magnitude  $\geq 3.0$ , for the ZnBZ method, in which  $d_f = 1.6$ , q = 0.5, b is the calculated b-value of the catalog (Fig. S1), and  $m_i$  is the magnitude of the triggering event. The clustered (lower left) and background (upper right) seismicity is partitioned by the common dashed white line in each panel. Only the clustered event pairs are retained in building event sequences.

all background rates. The likelihood and magnitude of time truncation of the true aftershock (and possibly foreshock) sequence increases with mainshock magnitude.

## Nearest-neighborhood linking—"ZnBZ"

An alternative way of isolating events in each cluster is the nearest-neighborhood method for linking earthquakes to parent events developed by Zaliapin and Ben-Zion (2013) using the metric proposed by Baiesi and Paczuski (2004). clusters Separation of achieved by first defining an overall decision boundary between background events and clustered events for each catalog. The separation of clustered and background is based on comparison with reshuffled catalogs without spatial-temporal seismicity clustering, which is analogous to the procedure in Zaliapin and Ben-Zion (2020) but at the whole catalog scale. We find the separation threshold (dashed lines in Fig. 2) from the 99th percentile of 100 random catalog representations. This method takes into account variations in seismicity density and background rates between the different regions. Figure 2 shows the separations between background and clustered seismicity in rescaled spatial and temporal dimensions for all the eight catalogs, along with decision lines separating the populations to the extent possible. Events in the lower left regions (below the dashed lines in Fig. 2) are retained in cluster analyses that link all foreshocks and aftershocks to the mainshocks sorted by event size.

This clustering approach, which we abbreviate as ZnBZ

for Zaliapin and Ben-Zion, is appealing in that it allows variable space and time windows from event to event without arbitrary a priori definition, notably allowing very long time windows to capture the extended tails of aftershock sequences following great earthquakes. However, as evident in Figure 2, there is likely some loss or contamination of clustered activity near the decision line, and discrete patches of both aftershock and foreshock activity sometimes fail to link to mainshocks for very large mainshocks, giving underestimates of the entire sequence productivity. High background seismicity in some catalogs such as for Inland Japan and Costa Rica is distinct from regions that have a preponderance of linked sequences (Italy, southern California, Greece, Alaska). Another attribute is that the isolated background events are intrinsically defined by the spatiotemporal characterization, distinct from the clustered sequences.

#### Magnitude-dependent time and space windowing —"TMC"

The third method provides a trade-off between the fixed time window approach of the WnC method and the ZnBZ clustering algorithm. ZnBZ is a purely event pair statistical approach without any physical conditioning on event linking. The time magnitude clustering (TMC) method gathers the clusters using a linkage algorithm prescribed by magnitude-dependent spatial and temporal distances following the widely used Gardner and Knopoff (1974) declustering method. Rather than using the original specific spatial and temporal conditions, tailored to southern California, we retain the basic approach of the Gardner and Knopoff formulation, while modifying the conditions for spatial and temporal distances. The spatial distance for triggering between earthquake pairs is the same as used for the WnC method (equation 1), and the temporal triggering window is defined by,

$$t = e^M, (2)$$

in which *t* is the time window (in days), similar to Knopoff *et al.* (1982). This results in triggering windows of 148, 403, 1096, 2980, and 8103 days for the magnitude range 5-9, all exceeding the 60-day window for the fixed-time procedure. We prohibit any negative temporal relation, constraining the earthquaketo-earthquake triggering mechanism. The time windows are generally comparable to the average durations of linked sequences for ZnBZ, although there are some fluctuations. For this method, clusters are defined in a cumulative fashion, in which the final duration and geographic size of each cluster are independent of fixed-spatial or -time windows, and do not associate exclusively with a specific mainshock (Fig. S2). Although the parameterization of this method still involves some arbitrary choices (as does the fixed-window WnC method), we show that it systematically captures the mainshock sequences for cases in which foreshocks or aftershocks extend beyond nominal 30-day and 60-day time windows, similarly to ZnBZ.

#### Mainshocks

In each earthquake cluster, mainshocks are typically readily identified as the largest magnitude event, separated on average over many events by ~1.2 magnitude units (Shearer, 2012) from the largest aftershock (and foreshock) events in the sequence, following Båth's law Båth (1965). However, there is a lot of spread in the Båth law parameter, and ambiguity is introduced when several relatively large events with similar magnitudes occur within the same cluster, generating earthquake doublets or triplets (e.g., Lay and Kanamori, 1980) or earthquake swarms when there are larger numbers of similar size large events. In such cases, foreshock and aftershock measures can be confounded by the sequential large earthquakes. There is always a finite potential for a triggered event to be as large or larger than the preceding large event, so these sequences are not statistically unexpected (Felzer et al., 2004); but they may represent regional conditions favorable to efficient triggering. Therefore, we use a set of rules for labeling clusters by the magnitude aperture between the largest events in each sequence. The largest earthquake (mainshock) is labeled  $M_1$ , and  $M_n$  is the *n*th largest in sorted order. In addition, we only consider mainshocks with  $M_{\rm w} \ge 5.0$ , a minimum of 2.0 units above our uniform  $M_{\rm c}$ , and with a total number of ≥4 events in a cluster apart from the mainshock. Each mainshock that has at least 0.5 magnitude units between  $M_1$  and  $M_2$  is labeled here as mainshock\*, which denotes a conventional mainshock sequence for which foreshocks can be most reliably characterized. The 0.5 magnitude difference allows for lower magnitude mainshocks to have somewhat lower aperture between  $M_1$  and  $M_2$  than for the strict average Båth law situation. Doublets, triplets, and two categories of swarm (swarm I and swarm 2) are defined as in the legend in Figure S3, using the size distribution of the four largest events in each sequence. Defining these categories using arbitrary but common sense parameters allows comparison of similar clear mainshock-type sequences from region to region.

In all the eight catalogs, the number of mainshocks\* before classification to cluster types is always larger for the WnC procedure than for the other two methods by up to a factor of  $\sim$ 2 (Fig. S3). After the classification for cluster types with at least five events in the sequence, the mainshock\* class yield more comparable numbers of mainshocks for the three methods ("Mainshocks\*" label in Fig. S3). Number of mainshocks\* varies from ~20 in northern California to ~100 in Turkey. Smaller seismicity clusters having less than four non-mainshock events systematically have much higher numbers for the WnC clustering method, mainly because there is no exclusion of background activity in the fixed-time window, so those sequences are not considered further.

#### **Foreshock Comparisons between** Methods

#### Spatial variations in foreshock count

Despite differences among individual sequences defined by the three methods (Fig. 3), especially for large events for which the

nearest neighborhood method (ZnBZ) can give much larger total aftershock counts (averaging from 2 to 7 times larger) than the magnitude-varying space + fixed-time windowing method (WnC), the procedures often result in comparable foreshock counts for moderate size mainshocks (e.g., Fig. 3a). The constant time-window method (WnC) usually gives larger estimates of the total number of foreshocks in regions of high background activity (e.g., Fig. 3b). It is challenging to evaluate whether the higher foreshock count for the WnC method for the Costa Rica event in Figure 3b is biased high by capturing background activity or the low foreshock count for the ZnBZ method is biased low by failure to link up events in diffuse foreshock activity. The TMC method clearly associated some of the prior activity to the mainshock, all of which is within the range of the effective radius. Aftershock counts are higher for the variable-time window methods within the source region effective radius because the allowed time after the mainshock exceeds the 60-day window in both Figure 3a and 3b; however, the basic duration of the sequences is generally compatible with the 60-day window. This is also true for most foreshock sequences for the 30-day window. Corresponding comparisons for all sequences along with the sequence classifications are shown in Figure Bundle S1 (see Data and Resources). No single procedure appears to be optimal for all cases, as there is no independent knowledge of true causal interactions between events.

### b-values of composite foreshock and aftershock sequences

Motivated by the previous studies indicating that b-values for foreshock populations may be lower than for aftershock populations, as proposed by Gulia and Wiemer (2019) in general and by Tamaribuchi et al. (2018) for Japan, we test for systematic differences between b-values of foreshock and aftershock sequences. It has long been recognized that measuring b-values of foreshocks relative to aftershocks is very dependent on data processing procedures (e.g., Knopoff et al., 1982), and attributing them to distinct physical processes before and after mainshocks is very tenuous if differences are reliably observed. The low number of foreshocks in the individual sequences prevents us from calculating meaningful b-values for each sequence. Therefore, we test for variations in b-values by comparing composite populations of foreshocks and aftershocks for mainshocks\* sequences for each of the eight catalogs using the ZnBZ clustering method (Fig. 4). The magnitude of completeness and the corresponding b-value parameters are calculated using the Kolmogorov-Smirnov test (see Fig. S1) with a magnitude bin size of 0.1.

Exclusion of the mainshock from b-value calculations for an aftershock sequence is a common practice, as mainshocks are considered to originate from a different Gutenberg–Richter distribution to account for typical Båth law parameters of about 1.2 (Console *et al.*, 2003; Shearer, 2012). We thus omit the mainshock values from the aftershock population (Fig. 4a)

and compute b-values using the maximum-likelihood method. We confirmed that including the mainshock magnitudes results in 0.0–0.2 lower b-values (Fig. 4b), even though the maximum-likelihood estimation procedure mitigates the effect. Therefore, to obtain a self-consistent measurement for the foreshock population, we select only foreshocks that occurred after the largest event in the foreshock sequences (Fig. 4a). The b-values for composite foreshock values are -0.1 to 0.7 units higher than when the largest foreshock and following foreshocks are considered (not shown) and when all foreshocks are retained (Fig. 4b), suggesting potential biasing when including the largest foreshock.

For northern California, Japan, Alaska, and Turkey, b-values of the composite foreshock sequences in Figure 4a are found to be 0.1–0.2 units lower that for the composite aftershock sequences. This is found consistently over a range of considered  $M_c$  levels (Fig. S4a). For southern California b-values of foreshocks and aftershock are the same using  $M_c$  3.4 and 3.2, respectively. However, when examining variations of b-value with  $M_c$ , the estimated b-value of foreshocks is lower than for aftershocks over most of the  $M_c$  range. The catalogs for Costa Rica and Greece did not include any cases with at least one earthquake after the largest event in the foreshock sequence. For Italy, the b-value of foreshock sequences is consistently higher at all  $M_c$  levels, but the dataset is sparse, and the b-value for foreshocks is not reliable (Fig. S4).

If we consider the entire foreshock population in Figure 4b, relative to the aftershock-only populations in Figure 4a, the foreshock *b*-values are lower in every case. Relative to the aftershock populations that include the mainshocks (Fig. 4b), four catalogs again result in lower *b*-values of composite foreshocks. Another concern is that whether the time duration used for foreshocks being shorter than that for most aftershock sequences biases properties of the corresponding Gutenberg–Richter distributions. We thus use the individual sequence time interval following the largest foreshock to the mainshock to constrain the length of the aftershock sequence considered in the composite distributions. This gives *b*-value estimates (Fig. S5) that are lower for foreshocks in three out of six regions.

To rule out the influence of the binning size on the *b*-value estimates (Marzocchi *et al.*, 2020), we tested the effect of the binning size of the magnitude range by examining a bin size of 0.2 (Fig. S6). The *b*-value estimates for 0.2 bin sizes are consistent with those for 0.1 bin size (Fig. 4).

We further search for differences in b-value of foreshock and aftershock sequences in a synthetic catalog generated by an ETAS model with a simple power law decay with distance following the algorithm of Brodsky (2011). We ran the WnC clustering algorithm over 10 yr of the synthetic catalog that includes 244,661 earthquakes with  $M_{\rm w} \ge 3$  and 2780  $M_{\rm w} \ge 5$ . Then, we used the same technique to compare the b-value of composite foreshock and aftershock sequences; foreshocks from the largest earthquake in the foreshock sequence to

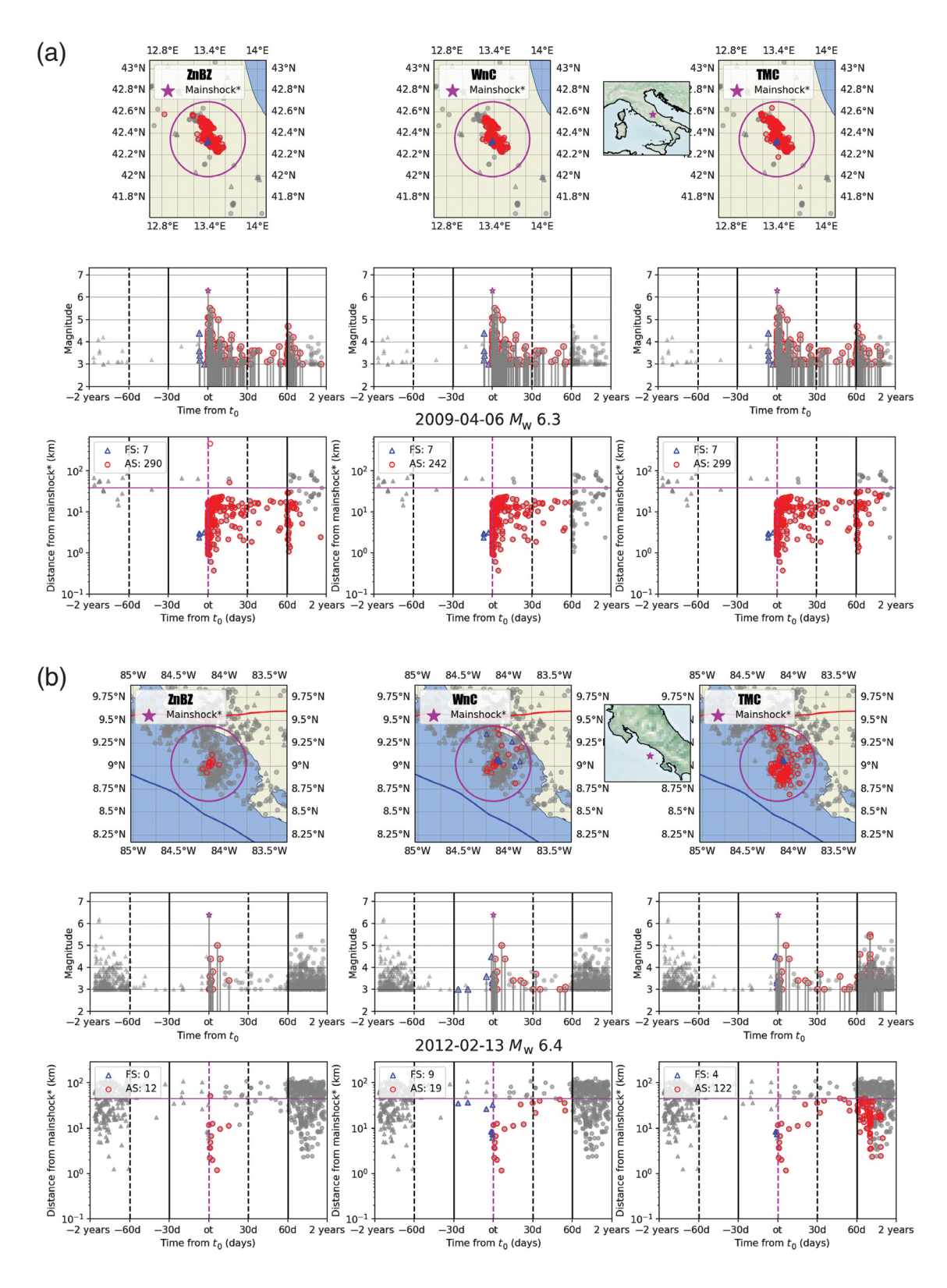
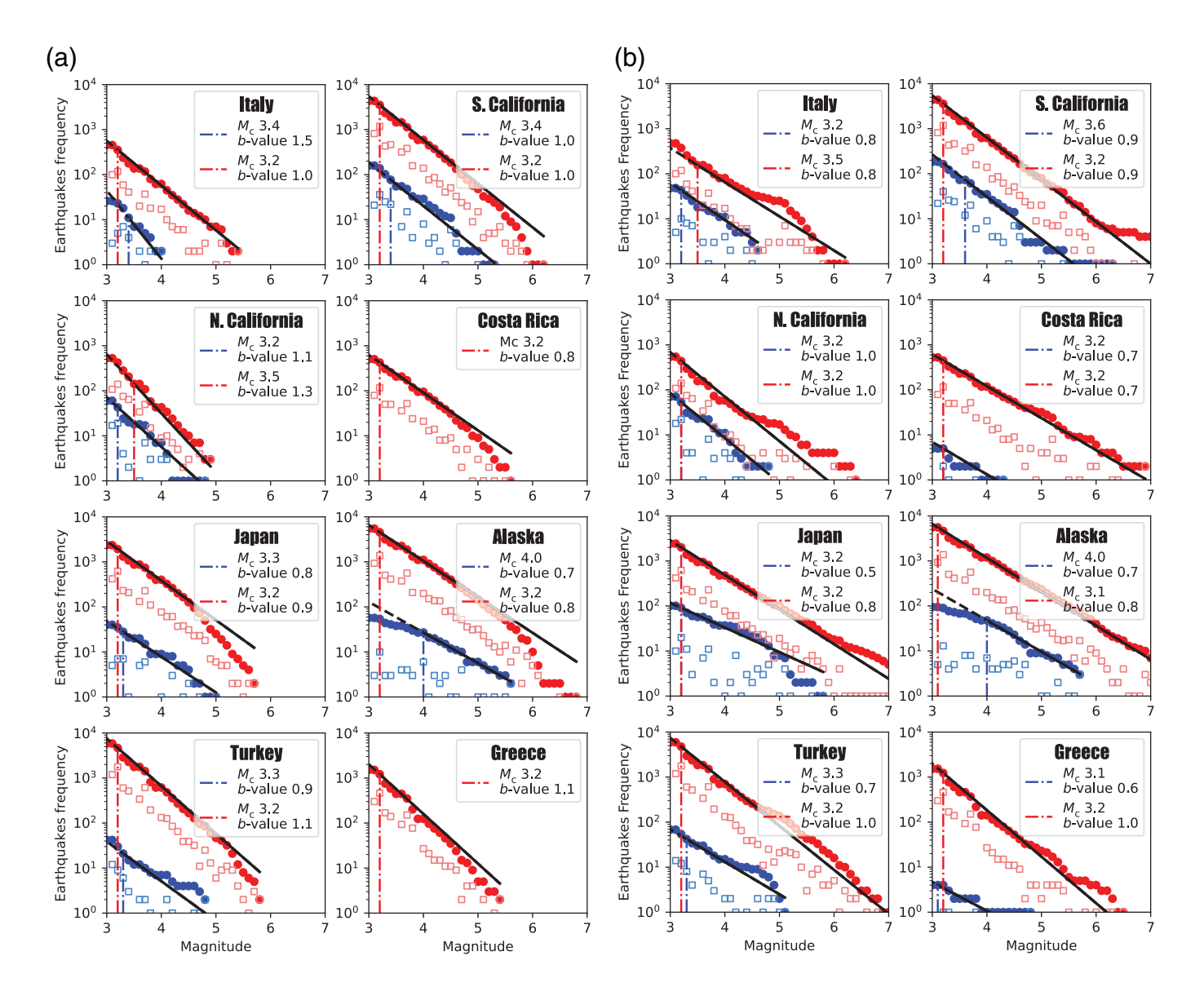


**Figure 3.** Example comparisons between the three clustering methods for (a) the 25 October 2009  $M_{\rm w}$  6.3 L'Aquila, Italy (mainshock\*), earthquake (see Data and Resources) and (b) the 13 February 2012  $M_{\rm w}$  6.4 Costa Rica (mainshock\*) earthquake sequence. Upper rows in each panel show map views of the seismicity with background events (gray) that occurred prior to the mainshock (triangles) or after (circles). The designated

foreshocks are plotted in blue and aftershocks in red. The magenta circles represent the effective radius of the mainshock (see equation 1). Time lines, with nonlinear scale, are shown for the seismicity in each map as functions of magnitude (middle row of each panel) and epicentral distance from the mainshock\* (lower row of each panel), with the same color scheme.



the mainshock and aftershocks (Fig. S7a1), and the entire foreshock sequence compared with aftershocks sequences with the corresponding mainshocks (Fig. S7b1). The analysis shows the same b-value for the foreshock and aftershock sequences over a range of  $M_c$  levels (Fig. S7a2,b2). The previous studies have shown that foreshocks in ETAS models have depressed bvalues relative to the general population (Helmstetter et al., 2003), because of an effect of conditioning the catalog when identifying the mainshocks. The mainshocks are most likely to happen after large-magnitude (and hence low b-value) foreshocks. However, the b-value of the foreshocks is not necessarily depressed relative to the aftershocks that immediately follow them, as the aftershocks have also been conditioned by the prior high seismicity rate. In addition, the b-value estimates in the ETAS calculations here are particularly stable due having robust populations combined with the maximum-likelihood estimation of b-value, as flattening of the distributions at high magnitudes has very limited affect on the slope estimates.

**Figure 4.** Magnitude distributions (open symbols) and the cumulative magnitude distribution (Gutenberg–Richter) relationships (filled symbols) determined for composite aftershock (red) and foreshock (blue) sequences for all eight catalogs, using the ZnBZ clustering algorithm. (a) The mainshock magnitudes are omitted from the aftershock distributions, and foreshocks are considered after the largest earthquake in the foreshock sequence to the origin time of the mainshock. (b) The entire composite foreshock sequence is compared with the composite aftershock sequence including the mainshocks. Maximum-like-lihood estimates are indicated by the black lines, and values are given in the inset. The variations of the b-value with respect to the selected  $M_c$  level are shown in Figure S4.

The exclusion of the largest events in *b*-value estimates for the foreshock and aftershock sequences is primarily motivated by the Båth law parameter, which measures the magnitude difference between the largest and next-largest event. Including the largest event when there is a large Båth law parameter flattens the distribution at high magnitude over a corresponding

interval, and this tends to reduce the b-value estimation. This effect is spread out for the composite populations, but some bias will persist. The Båth law parameters for our mainshock\* sequences show typical large average parameters of 1.25-1.45 for mainshocks—the largest aftershocks, but systematically lower values of 0.4–0.7 for the largest foreshock—following next large foreshock (Fig. S8). It is important to see that there is a lot of scatter in Båth law parameters for both foreshock and aftershock sequences, with our aftershock populations having a lower cutoff at 0.5. The reduced Båth law parameters for the foreshock sequences suggest that there should be less bias in bvalue estimates when the largest foreshock is included relative to the effect of having mainshocks in the aftershock population. However, the ETAS simulations also gave lower Båth law parameters for the foreshocks with no bias in the b-value estimation (Fig. S7c), so the low parameters for foreshocks are likely controlled by the distribution cutoff at  $M_c$  3.

#### Foreshock occurrence rates

The percentage of mainshocks\* with foreshocks in each catalog for our uniform completeness magnitude is indicated by the bar diagrams in Figure 5 for three levels: mainshocks without detected foreshocks (white portions), mainshocks with 1-4 foreshocks (light-blue portions), and mainshocks with ≥5 foreshocks (dark-blue portions). Foreshock counts are based on the cluster spatial and temporal window conditions of each method. The three clustering methods detect at least one foreshock with occurrence probabilities ranging between 14% and 72% for mainshocks\* (Fig. 5a). Most foreshocks are detected within the 30-day time window prior to the mainshock for all methods (Fig. 5b), and most are located within the effective radius of the mainshock defined by the WnC method (e.g., Fig. 3). For all regional composite cases, WnC estimates more foreshocks than the ZnBZ and TMC methods, although the ZnBZ and TMC methods are able to link temporally and spatially remote foreshocks (and aftershocks activity), beyond the dimension of the mainshock's effective rupture length (Fig. S9). This is particularly pronounced for regions with high background activity (high concentrations in the upper right partitions in each panels of Fig. 2). For example, for Costa Rica, the probability for having at least one foreshock ranges from 41% with the ZnBZ method, to 14% for the TMC method, and to 63% for the WnC method. Italy is found to have the most productive foreshock occurrences for the time-varying methods, with 43%-56% of mainshocks\* having at least a single foreshock.

Imposing a constant aperture level of 2.0 magnitude units below the mainshock magnitude should theoretically equalize the measurements for different magnitude ranges spanned by each catalog (Fig. 5c). The percentages of mainshocks\* with foreshocks decrease in most catalogs by 10%–20%, and this is mostly pronounced for the WnC method, making the percentages more similar between the methods, as expected.

In southern California, the percentages of foreshock occurrence above  $M_c$  range between 48% (ZnBZ) and 44% (TMC), comparable to the previous study of Chen and Shearer (2016) but  $\sim$ 25% lower than the study by Trugman and Ross (2019), which proposed that 72% of the mainshocks were preceded by foreshocks in the same region based on a higher resolution catalog constructed using template matching. Trugman and Ross (2019) suggested that their high level of foreshocks was due to the unusually low  $M_c$  (~1.0), but van den Ende and Ampuero (2020) argued that the foreshock rate should be revised downward after accounting for background activity fluctuations. This controversy revolves around the specifics of the catalog used by Trugman and Ross but is tangential to this study, because our focus here is on the observability of foreshocks in conventional catalogs that have higher  $M_c$ , which has operational significance and comparative value.

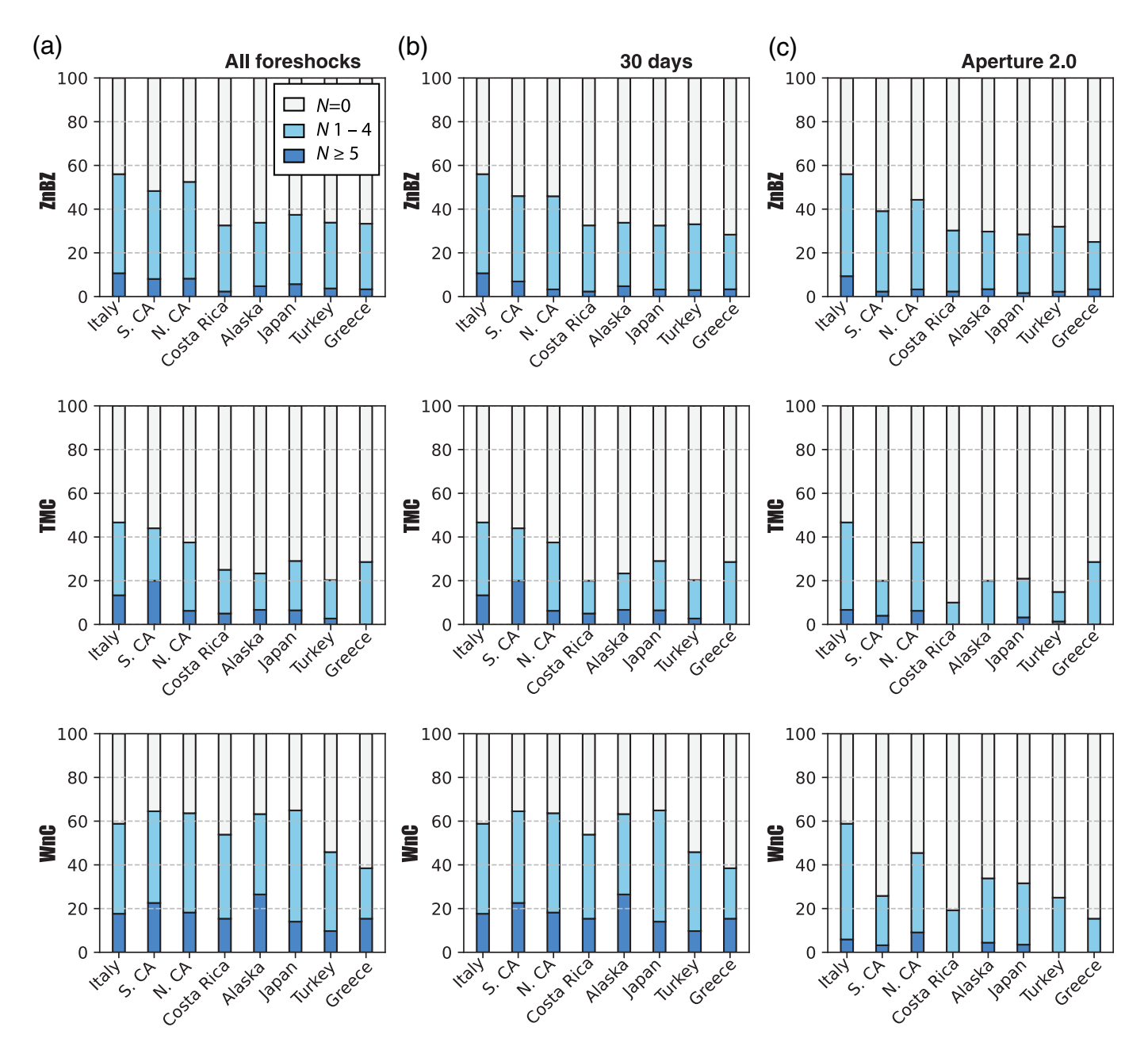
For onshore Japan we find that 37% of mainshock\* were preceded by foreshocks above  $M_c$  using the ZnBZ, consistent with the results of Tamaribuchi *et al.* (2018) using a similar method. However, the percentages increase by a factor of 2 using the WnC method, likely due to contamination by the high background levels in Japan (Fig. 2).

#### Foreshocks and background seismicity

Relatively large spatial variations in background rate across convergent plate boundaries were recognized by Habermann *et al.* (1986), and were later revisited and associated with mechanical processes such as subduction zone slab bending angle (Nishikawa and Ide, 2015). Variations in the background seismicity were also associated with geomorphological changes of the Peru–Chile and Japan margins (Madella and Ehlers, 2021). Background rate variations can be associated with heterogeneity in the regional and local stress fields (Scholz, 2015), as well as the mechanical properties in which these events nucleate.

The characterization of the background seismicity by ZnBZ clearly shows variations between the different regions (Fig. 2); the percentage of the background seismicity relative to the entire catalog ranges between 65% in Costa Rica and 25% in southern California (Fig. 6a). Therefore, it might be expected from the Gutenberg–Richter distribution (e.g., Fig. S1) that high background rates should yield more frequent foreshock activity. However, it is also proposed that foreshocks are controlled by fault-strength heterogeneity and are associated with weaker fault regions at the periphery of the primary asperity (Kanamori, 1981). Comparing background rates with foreshock probabilities shows that probability of observable foreshocks preceding mainshocks\* decreases as the percentage of regional background seismicity increases (Fig. 6b).

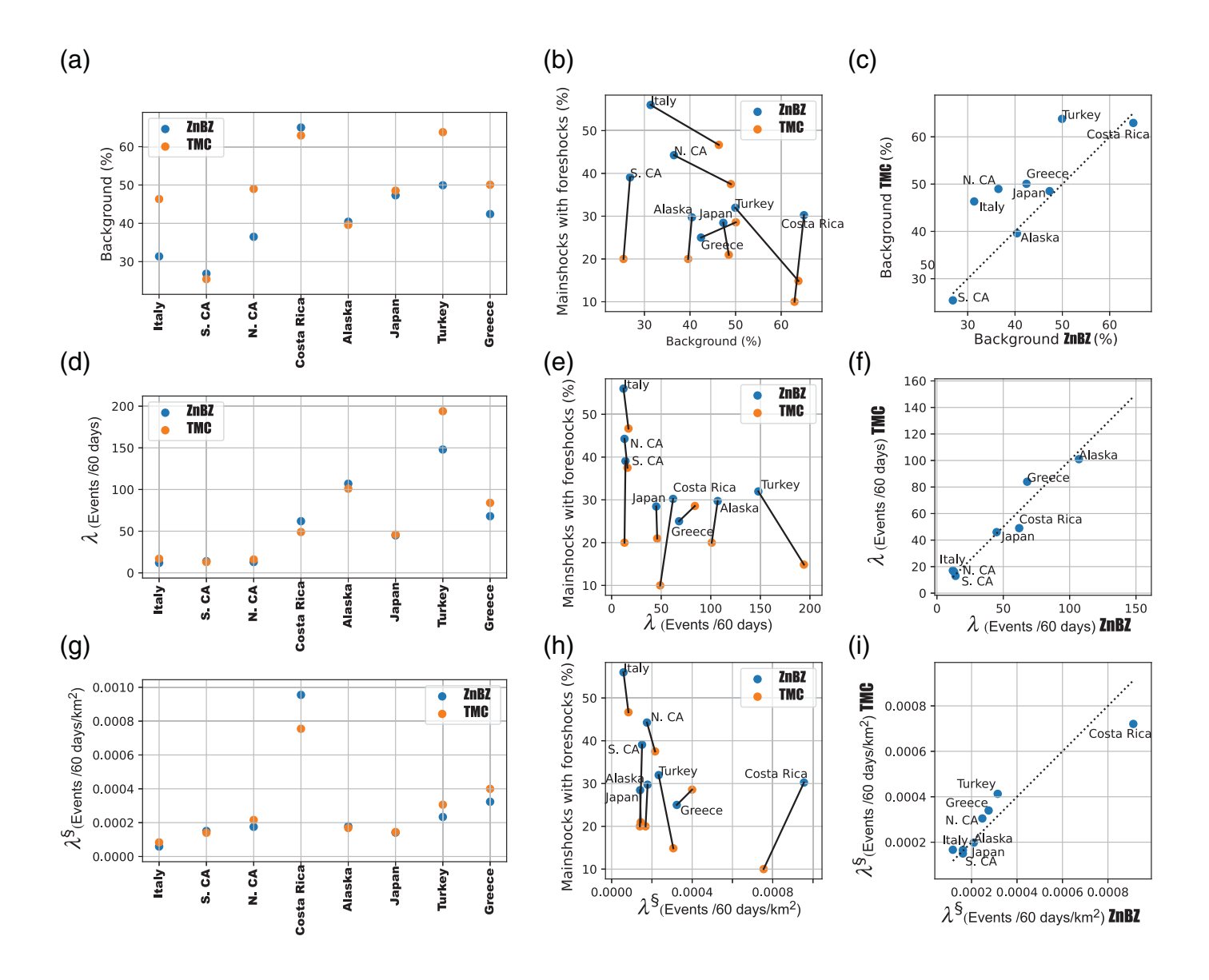
To further investigate the relationship between background seismicity and foreshock occurrence, we represent the regional background rates by fitting the declustered TMC and ZnBZ catalogs with a Poissonian statistical model (Figs. S10 and S11, respectively). Values of the estimated seismicity rate,  $\lambda$ 



(Poissonian parameter representing the mean number of background earthquakes per 60 days), range between 20 in Italy and ~200 in Turkey (Fig. 6d). In a similar fashion to behavior of the percentage of the background (Fig. 6b), increasing background rate,  $\lambda$ , also decreases the percentage of mainshock\* (Fig. 6e) preceded by foreshocks considering only earthquakes within 2.0 magnitude units below the mainshock magnitude (Fig. 5c). We observe that both clustering methods show nonstationary background distributions for Turkey. The seismicity rate,  $\lambda$ , changes between 2002 and 2012. Nas *et al.* (2019) tested eight different declustering algorithms on the Turkish catalog and concluded that none of the declustering methods were able to produce a declustered catalog that follows a temporally homogeneous Poisson process.

To provide a comparable measurement of the seismicity rates, we normalize the background seismicity rates by the seismogenic

**Figure 5.** Percentage of mainshock\* events (classified in Fig. S3) with foreshocks (colored portions of histograms: dark blue indicates number of foreshocks ≥5, and light blue indicates number of foreshocks from 1 to 4) and without foreshocks (white portions of histograms) for the eight catalogs, considering all earthquakes above the uniform completeness magnitude,  $M_c$  3.0 for the three clustering methods: the nearest-neighbor linking (ZnBZ), time and distance magnitude-dependent linking method (TMC), and the magnitude-dependent spatial with 30 days temporal windowing (WnC). The number of foreshocks is determined for three cases: (a) using all foreshocks in each individual cluster, (b) imposing a constant 30-day time window, and (c) considering only earthquakes within 2.0 magnitude units below the mainshock magnitude.



area of each region. Seismogenic areas for the ZnBZ (Fig. S12) and TMC (Fig. S13) background populations are estimated for a regular grid of 0.5°, with the number of earthquakes from each declustered catalog with  $M_{\rm c} \geq 3.0$  counted in each grid cell. The area is integrated over grid cells having a number of earthquakes larger than 10% of the maximum value of the gridded seismicity. The regional seismicity rate areal densities,  $\lambda$  (Fig. 6g) show a comparable trend with the  $\lambda$  results; increasing background seismicity density tends to decrease regional foreshock activity (Fig. 6h).

An alternative and complementary comparison of the background measurement to the probability of having foreshocks is provided by characterizing the seismicity rate by the mainshock\* rate (number of mainshocks\* per year, Fig. S14). The mainshock\* rate varies between 0.5 in Italy and 7.5 mainshocks\* per year in Alaska (Fig. S14a1). Once rates are normalized for seismicity area (mainshocks\*) for the ZnBZ and TMC clusters (Figs. S12 and S13), the mainshock\* rates equalized to  $\sim 1 \times 10^{-5}$  mainshock\* per year

Figure 6. (a) Percentage of background seismicity (% of the total catalog) is shown in each catalog for the ZnBZ and TMC clustering algorithms. (b) The background level is plotted versus the percentage of mainshocks\* with foreshocks considering only earthquakes within 2.0 magnitude units below the mainshock magnitude (Fig. 5c) for each catalog and (c) in a 1:1 plot of the measures for the two clustering algorithms. (d) The estimated seismicity rate,  $\lambda$  (number of background earthquakes per 60 days), is shown for the ZnBZ and TMC clustering algorithms. (e) The Poisson parameter  $\lambda$  is plotted versus the percentage of mainshocks\* (Fig. 5c) with foreshocks for each catalog and (f) in a comparison 1:1 plot of the two clustering algorithms. (g) The estimated seismicity rate density,  $\lambda^{\mathbb{S}}$  (number of background earthquakes per 60 days per km<sup>2</sup>), is shown for the ZnBZ and TMC clustering algorithms. (h)  $\lambda^{\mathbb{S}}$  is normalized by the seismogenic area for each region (Figs. S10 and S11) and is plotted versus the percentage of mainshocks\* with foreshocks (Fig. 5c) for each catalog and (i) in a comparison 1:1 plot of the measures for the two clustering algorithms.

per km² (Fig. S14b1), except for Costa Rica. In a similar fashion to increasing background seismicity with decreasing regional foreshock activity (Fig. 6b), as the mainshock\* rates for ZnBZ and TMC clustering methods increase, there is a decreasing percentage of mainshocks\* with foreshocks (Fig. S14a2). The trend is preserved for the measurements normalized by the seismogenic area (Fig. S14b2). The similarity between mainshock\* rates (Fig. S14) and the background seismicity rates (Fig. 6) compared with the percentage of mainshocks\* with foreshocks can be predicted from the Gutenberg–Richter relationship. Naturally, regions with high background rate result in more mainshocks\* (Fig. S14c1,c2).

The variation of foreshock occurrence with background rate (or mainshock\* rate) seen in Figure 6 (and Fig. S14) are a different effect than the variation of foreshock counts between clustering methods. The WnC approach makes no correction for background occurrence, but sweeps up all events in the designated space-time window, yielding higher total counts, and this effect is thus enhanced in regions with higher background rates. The trends in Figure 6 instead indicate that when background levels are low, there is a higher likelihood of detecting foreshocks for the linking methods, which suggests that stress heterogeneities prior to a mainshock have not been released by background activity, and the stress buildup prior to failure drives the foreshock sequence. Regions that have high background activity may have distributions of heterogeneities with lower strengths that do not require high stress accumulations to fail.

To further safeguard against misinterpreting background activity as foreshocks that are physically related to the eventual mainshock, we compare the foreshock and aftershock rates to the background rates. Should the foreshock rate be comparable with the background rate, such confusion might occur. For each mainshock we calculated the mean background, foreshock, and aftershock rates in a circular area with a radius defined by the maximum epicentral distance of the cluster from the mainshock. The time windows of the background rates are calculated for each individual sequence, defined from the beginning of each catalog to the first foreshock. The time windows used for calculating the rates for foreshock and aftershock sequences are defined by the individual duration of each sequence.

We then examine the distribution of the resulting ratios between foreshock and background rates for each mainshock as well as the aftershock to background ratio (Fig. S15). We use these data to measure the percentage of the sequences showing low foreshock-to-background (<1) ratios. Typically, the aftershock sequence rates are relatively higher than the foreshock rates, with only a few cases for which the measured aftershocks rates are lower than the background rates. For the foreshocks, in most of the catalogs (southern California, northern California, Italy, Alaska, and Turkey), we find that only 0%–6% of the foreshock sequences show rates that are lower

than the background rates. The maximum percentage of lowrate foreshock sequences, 22%, is found in Japan. It is possible that the background rates for Japan are biased by the choice of the spatial windows and the inclusion of peripheral seismicity, affecting also the measurement of the equivalent rates measured for the aftershock sequences. We conclude that most foreshock rates are larger than background rates and thus are reasonably interpreted as linked to the subsequent mainshock.

#### Foreshocks effects on aftershocks productivity

Cascade-type models are built on the thesis that foreshocks and aftershocks are outcomes of the same process (e.g., Ogata, 1988). Support for this framework is provided by the previous work that showed mainshocks with foreshocks tend to result in more aftershocks (Marsan et al., 2014). Although our dataset is not ideal to directly address the cascade model, contextualization in the light of the previous work is helpful. Such a comparison first needs to normalize for mainshock magnitude. We therefore follow the previous work and measure the aftershocks productivity parameter K for each catalog, assuming a constant power law K = 1 for  $N_{\text{aft}} = K10^{\alpha(M-M_c)}$  (e.g., Reasenberg and Jones, 1989). We see that mainshocks\* with foreshocks tend to result in more aftershocks when there are sufficient numbers of events with foreshocks (shown for the ZnBZ method in Fig. S16). This observation is consistent with Marsan et al. (2014) and a cascade interpretation. However, when we compare the percentage of mainshocks\* with foreshocks to aftershocks productivity using the ZnBZ method (Fig. S17), we find no clear correlation. This result may suggest that at least some foreshock processes are distinct from mechanisms associated with mainshock-aftershock triggering. Such an interpretation is consistent with other studies, which imply that some, but not all, foreshocks are due to aseismic slip (e.g., Moutote et al., 2021).

Another aspect of the influence of foreshocks on the aftershock sequence can be observed by comparing aftershocks sequences of mainshocks\* with and without foreshocks (Fig. S18). To first order, as the foreshock sequence decays, magnitudes also decrease with time. Therefore, the interference of the foreshocks Omori tail in the aftershocks sequence is predicted to affect the low magnitude range, which should increase the *b*-value of aftershocks sequences compared with sequences that were not preceded by foreshocks. However, by this argument the foreshock sequence itself should increase in *b*-value as it progresses, which is not evident in Figure 4. This can be associated with accelerated rates toward the mainshock, commonly observed by stacked foreshock sequences as an inverse Omori law (e.g., Reasenberg, 1999).

#### **Conclusions**

The general characteristics of foreshock activity for eight catalogs is quantified using three clustering methods. To obtain a generalizable count of foreshocks, the selection of mainshocks

takes into consideration any biasing from swarms, doublets, or triplets clusters, focusing on clear mainshock-type sequences. We show that b-values for composite foreshock distributions are lower than for composite aftershocks for a space-time clustering algorithm for all the eight regions, but the difference is reduced, although still present, for four out of six regions, when omitting the largest foreshock. We observe clear regional trends in foreshock probabilities (for events within 2 magnitude units of the mainshocks), which range, for example, from 47% to 60% in Italy to 10% to 35% in Costa Rica. Those regional variations for magnitude aperture 2 are compared with variations in the background rates normalized by seismogenic area, indicating that regions of relatively low background seismicity tend to have higher foreshock activity for linkingbased approaches, albeit with substantial scatter. This observation suggests that a lower background rate may manifest in a higher occurrence rate of observable foreshocks, possibly due to unrelieved stress accumulation in the region of future mainshocks. Overall, identification of foreshock activity is found to be sensitive to the clustering method, with no single procedure appearing to be optimal for all the cases. However, clustering methods with an adaptive time window appear to perform better in capturing the "true" foreshock-aftershock sequence, especially in regions of relatively high background rates.

#### **Data and Resources**

Earthquake data for California were accessed through Northern California Earthquake Data Center (NCEDC; DOI: 10.7932/NCEDC) and Southern California Earthquake Data Center (SCEDC; DOI: 10.7909/C3WD3xH1). For Turkey, we used the earthquake catalog of Tan (2021). The earthquake catalog of Italy is obtained from Lolli et al. (2020). The Japan earthquake catalog was accessed from the Japan Meteorology Agency (JMA; https://www.data.jma.go.jp/svd/eqev/data/ bulletin/hypo\_e.html, last accessed December 2020). The Costa Rica catalog is obtained from https://www.data.jma.go.jp/svd/eqev/data/bulletin/ hypo\_e.html (last accessed October 2021). The Alaska-Aleutians earthquake catalog was accessed using the U.S. Geological Survey-National Earthquake Information Center (USGS-NEIC) earthquake catalog, which draws from the Alaska Seismic Network operated by the Alaska Earthquake Center (DOI: 10.7914/SN/AK). Earthquake catalog of Greece was accessed using the National Observatory of Athens earthquake catalog (https://www.gein.noa.gr/services/cat.html, last accessed March 2021). The maps in this article were made by the Matplotlib (Hunter, 2007). Code for calculating the Gutenberg-Richter magnitude distribution is available at https://github.com/tgoebel/magnitudedistribution (last accessed March 2022). The TMC algorithm is available at https://github.com/nadavwetzler/TMC (last accessed March 2021). The workflow and detailed explanations of the nearest-neighbor clustering method by Zaliapin and Ben-Zion (2013) are available at https:// github.com/tgoebel/clustering-analysis (last accessed March 2021). The 25 October 2009  $M_{\rm w}$  6.3 L'Aquila, Italy, earthquake data are available at http://terremoti.ingv.it/en/event/1895389 (last accessed September 2021). The supplemental material for this article includes 18 figures and figure bundle S1 available at https://figshare.com/articles/figure/ Figure\_Bundle\_S1/20115947 (last accessed June 2022).

#### **Declaration of Competing Interests**

The authors acknowledge that there are no conflicts of interest recorded.

#### **Acknowledgments**

This research was supported by Grant 2017683 from the United States—Israel Binational Science Foundation (BSF) and by the Department of Energy Basic Energy Science Program Grant 0000242877 and EAR-1761987 from the U.S. National Science Foundation (NSF). Thorne Lay's research on earthquake processes is supported by the U.S. NSF Grant EAR-1802364. The authors thank *SRL* Editor Allison Bent, two anonymous reviewers, and Andy Michael for their useful comments that improved this article.

#### References

- Baiesi, M., and M. Paczuski (2004). Scale-free networks of earthquakes and aftershocks, *Phys. Rev. E* 69, no. 6, doi: 10.1103/PhysRevE. 69.066106.
- Båth, M. (1965). Lateral inhomogeneities of the upper mantle, *Tectonophysics* **2**, 483–514, doi: 10.1016/0040-1951(65)90003-X.
- Bird, P. (2003). An updated digital model of plate boundaries, *Geochem. Geophys. Geosys.* **4,** doi: 10.1029/2001GC000252.
- Brodsky, E. E. (2011). The spatial density of foreshocks, *Geophys. Res. Lett.* **38**, no. 10, L10305, doi: 10.1029/2011GL047253.
- Brodsky, E. E., and T. Lay (2014). Recognizing foreshocks from the 1 April 2014 Chile earthquake, *Science* **344**, 700–702, doi: 10.1126/science.1255202.
- Chen, X., and P. M. Shearer (2016). Analysis of foreshock sequences in California and implications for earthquake triggering, *Pure Appl. Geophys.* 173, 133–152, doi: 10.1007/s00024-015-1103-0.
- Console, R., A. M. Lombardi, M. Murru, and D. Rhoades (2003). Båth's law and the self-similarity of earthquakes, *J. Geophys. Res.* **108**, 2128, doi: 10.1029/2001JB001651.
- Dascher-Cousineau, K., E. E. Brodsky, T. Lay, and T. H. W. Goebel (2020). What controls variations in aftershock productivity? *J. Geophys. Res.* **125**, no. B1, doi: 10.1029/2019JB018111.
- Felzer, K. R., R. E. Abercrombie, and G. Ekstrom (2004). A common origin for aftershocks, foreshocks, and, multiplets, *Bull. Seismol. Soc. Am.* **94**, 88–98, doi: 10.1785/0120030069.
- Gardner, J. K., and L. Knopoff (1974). Is the sequence of earthquakes in southern California, with aftershocks removed, Poissonian? *Bull. Seismol. Soc. Am.* 64, 1363–1367.
- Goebel, T. H. W., G. Kwiatek, T. W. Becker, E. E. Brodsky, and G. Dresen (2017). What allows seismic events to grow big? Insights from b-value and fault roughness analysis in laboratory stick-slip experiments, *Geology* **45**, 815–818, doi: 10.1130/G39147.1.
- Gulia, L., and S. Wiemer (2019). Real-time discrimination of earth-quake foreshocks and aftershocks, *Nature* **574**, 193–199, doi: 10.1038/s41586-019-1606-4.
- Habermann, R. E., W. R. McCann, and B. Perin (1986). Spatial seismicity variations along convergent plate boundaries, *Geophys. J. R. Astron. Soc.* **85**, 43–68, doi: 10.1111/j.1365-246X.1986.tb05171.x.
- Hasegawa, A., K. Yoshida, Y. Asano, T. Okada, T. Iinuma, and Y. Ito (2012). Change in stress field after the 2011 great Tohoku-Oki earthquake, *Earth Planet. Sci. Lett.* 355–356, 231–243, doi: 10.1016/ j.epsl.2012.08.042.

- Helmstetter, A., and D. Sornette (2003). Foreshocks explained by cascades of triggered seismicity, *J. Geophys. Res.* **108**, no. B10, doi: 10.1029/2003JB002409.
- Helmstetter, A., D. Sornette, and J.-R. Grasso (2003). Mainshocks are aftershocks of conditional foreshocks: How do foreshock statistical properties emerge from aftershock laws, *J. Geophys. Res.* **108**, 2046, doi: 10.1029/2002JB001991.
- Hunter, J. D. (2007). Matplotlib: A 2D graphics environment, *Comput. Sci. Eng.* **9**, no. 3, 90–95, doi: 10.1109/MCSE.2007.55.
- Jones, L., and P. Molnar (1976). Frequency of foreshocks, *Nature* 262, 677–679.
- Kanamori, H. (1981). The nature of seismicity patterns before large earthquakes, in *Earthquake Prediction: An International Review*, *Maurice Ewing Series*, D. W. Simpson and P. G. Richards (Editors), Vol. 4, American Geophysical Union, Washington, D. C., 1–19.
- Kato, A., and T. Igarashi (2012). Regional extent of the large coseismic slip zone of the 2011 Mw 9.0 Tohoku-Oki earthquake delineated by on-fault aftershocks, *Geophys. Res. Lett.* **39**, 2–7, doi: 10.1029/2012GL052220.
- Knopoff, L., Y. Y. Kagan, and R. Knopoff (1982). b values for fore-shocks and aftershocks in real and simulated earthquake sequences, Bull. Seismol. Soc. Am. 72, 1663–1676.
- Lay, T., and H. Kanamori (1980). Earthquake doublets in the Solomon Islands, *Phys. Earth Planet. In.* **21**, 283–304, doi: 10.1016/0031-9201(80)90134-X.
- Lolli, B., D. Randazzo, G. Vannucci, and P. Gasperini (2020). The homogenized instrumental seismic catalog (HORUS) of Italy from 1960 to present, *Seismol. Res. Lett.* 91, 3208–3222, doi: 10.1785/ 0220200148.
- Madella, A., and T. A. Ehlers (2021). Contribution of background seismicity to forearc uplift, *Nat. Geosci.* **14,** 620–625, doi: 10.1038/s41561-021-00779-0.
- Marsan, D., A. Helmstetter, M. Bouchon, and P. Dublanchet (2014). Foreshock activity related to enhanced aftershock production, *Geophys. Res. Lett.* **41,** no. 19, 6652–6658, doi: 10.1002/2014GL061219.
- Marzocchi, W., I. Spassiani, A. Stallone, and M. Taroni (2020). How to be fooled searching for significant variations of the b-value, *Geophys. J. Int.* **220**, no. 3, 1845–1856, doi: 10.1093/gji/ggz541.
- Mignan, A. (2014). The debate on the prognostic value of earthquake foreshocks: A meta-analysis, *Sci. Rep.* **4**, doi: 10.1038/srep04099.
- Mizrahi, L., S. Nandan, and S. Wiemer (2021). The effect of declustering on the size distribution of mainshocks, *Seismol. Res. Lett.* **92**, 2333–2342, doi: 10.1785/0220200231.
- Moutote, L., D. Marsan, O. Lengliné, and Z. Duputel (2021). Rare occurrences of non-cascading foreshock activity in southern California, *Geophys. Res. Lett.* **48**, doi: 10.1029/2020GL091757.
- Nas, M., A. Jalilian, and Y. Bayrak (2019). Spatiotemporal comparison of declustered catalogs of earthquakes in Turkey, *Pure Appl. Geophys.* **176**, 2215–2233, doi: 10.1007/s00024-018-2081-9.
- Nishikawa, T., and S. Ide (2015). Background seismicity rate at subduction zones linked to slab-bending-related hydration, *Geophys. Res. Lett.* **42**, 7081–7089, doi: 10.1002/2015GL064578.
- Ogata, Y. (1988). Statistical models for earthquake occurrences and residual analysis for point processes, *J. Am. Stat. Assoc.* **83**, 9–27, doi: 10.1080/01621459.1988.10478560.

- Persh, S. E., and H. Houston (2004). Strongly depth-dependent after-shock production in deep earthquakes, *Bull. Seismol. Soc. Am.* **94**, 1808–1816, doi: 10.1785/012003191.
- Reasenberg, P. A. (1999). Foreshock occurrence before large earth-quakes, *J. Geophys. Res.* **104**, 4755–4768, doi: 10.1029/1998jb900089.
- Reasenberg, P. A., and L. M. Jones (1989). Earthquake hazard after a mainshock in California, *Science* **243**, 1173–1176, doi: 10.1126/science.243.4895.1173.
- Ruiz, S., M. Metois, A. Fuenzalida, J. Ruiz, F. Leyton, R. Grandin, C. Vigny, R. Madariaga, and J. Campos (2014). Intense foreshocks and a slow slip event preceded the 2014 Iquique Mw8.1 earthquake, *Science* 345, 1165–1169, doi: 10.1126/science.1256074.
- Scholz, C. H. (2015). On the stress dependence of the earthquake b value, Geophys. Res. Lett. 42, 1399–1402, doi: 10.1002/2014GL062863.
- Shearer, P. M. (2012). Self-similar earthquake triggering, Båth's law, and foreshock/aftershock magnitudes: Simulations, theory, and results for southern California, J. Geophys. Res. 117, doi: 10.1029/ 2011JB008957.
- Shi, Y., and B. Bolt (1982). The standard error of the magnitude-frequency b-value, *Bull. Seismol. Soc. Am.* **72**, 1677–1687.
- Singh, S. K., and G. Suárez (1988). Regional variation in the number of aftershocks ( $m_b \ge 5$ ) of large, subduction-zone earthquakes ( $M_w \ge 7.0$ ), *Bull. Seismol. Soc. Am.* **78**, 230–242.
- Tahir, M., and J. R. Grasso (2015). Faulting style controls for the space–time aftershock patterns, *Bull. Seismol. Soc. Am.* **105**, 2480–2497, doi: 10.1785/0120140336.
- Tamaribuchi, K., Y. Yagi, B. Enescu, and S. Hirano (2018). Characteristics of foreshock activity inferred from the JMA earth-quake catalog, *Earth Planets Space* **70**, 90, doi: 10.1186/s40623-018-0866-9.
- Tan, O. (2021). A homogeneous earthquake catalogue for Turkey, Nat. Hazards Earth Syst. Sci. 21, 2059–2073, doi: 10.5194/ nhess-21-2059-2021.
- Trugman, D. T., and Z. E. Ross (2019). Pervasive foreshock activity across southern California, Geophys. Res. Lett. doi: 10.1029/ 2019GL083725
- Utsu, T. (1970). Aftershocks and earthquake statistics (1): Some parameters which characterize an aftershock sequence and their interrelations, *J Faculty Sci Hokkaido Univ. Ser 7 Geophys.* 3, no. 3, 129–195.
- Utsu, T., Y. Ogata, and S. R. Matsu'ura (1995). The centenary of the Omori formula for a decay law of aftershock activity, *J. Phys. Earth* **43**, no. 1, 1–33, doi: 10.4294/jpe1952.43.1.
- van den Ende, M. P. A., and J. P. Ampuero (2020). On the statistical significance of foreshock sequences in southern California, *Geophys. Res. Lett.* **47**, doi: 10.1029/2019GL086224.
- Wells, D. L., and K. J. Coppersmith (1994). New empirical relationships among magnitude, rupture length, rupture width, rupture area, and surface displacement, *Bull. Seismol. Soc. Am.* 84, 974– 1002, doi: 10.1785/BSSA0840040974.
- Wetzler, N., E. E. Brodsky, and T. Lay (2016). Regional and stress drop effects on aftershock productivity of large megathrust earthquakes, *Geophys. Res. Lett.* **43**, 12,012–12,020, doi: 10.1002/2016GL071104.
- Wetzler, N., T. Lay, E. E. Brodsky, and H. Kanamori (2017). Rupture-depth-varying seismicity patterns for major and great ( $M_{\rm w} \geq 7.0$ ) megathrust earthquakes, *Geophys. Res. Lett.* **44**, 9663–9671, doi: 10.1002/2017GL074573.

- Wetzler, N., T. Lay, E. E. Brodsky, and H. Kanamori (2018). Systematic deficiency of aftershocks in areas of high coseismic slip for large subduction zone earthquakes, *Sci. Adv.* **4**, doi: 10.1126/sciadv.aao3225.
- Zaliapin, I., and Y. Ben-Zion (2013). Earthquake clusters in southern California II: Classification and relation to physical properties of the crust, *J. Geophys. Res.* **118**, 2865–2877, doi: 10.1002/jgrb.50178.
- Zaliapin, I., and Y. Ben-Zion (2020). Earthquake declustering using the nearest-neighbor approach in space-time-magnitude domain, *J. Geophys. Res.* **125**, no. 4, doi: 10.1029/2018JB017120.

Manuscript received 16 April 2022 Published online 26 October 2022

#### Supporting Online Material for

### Regional characteristics of observable foreshocks

Nadav Wetzler\*, Emily E. Brodsky, Esteban J. Chaves, Thomas Goebel, and Thorne Lay

\* To whom correspondence should be addressed. E-mail: <a href="mailto:nadavw@gsi.gov.il">nadavw@gsi.gov.il</a>

This file includes: Eighteen supporting figures and a caption for figure bundle S1

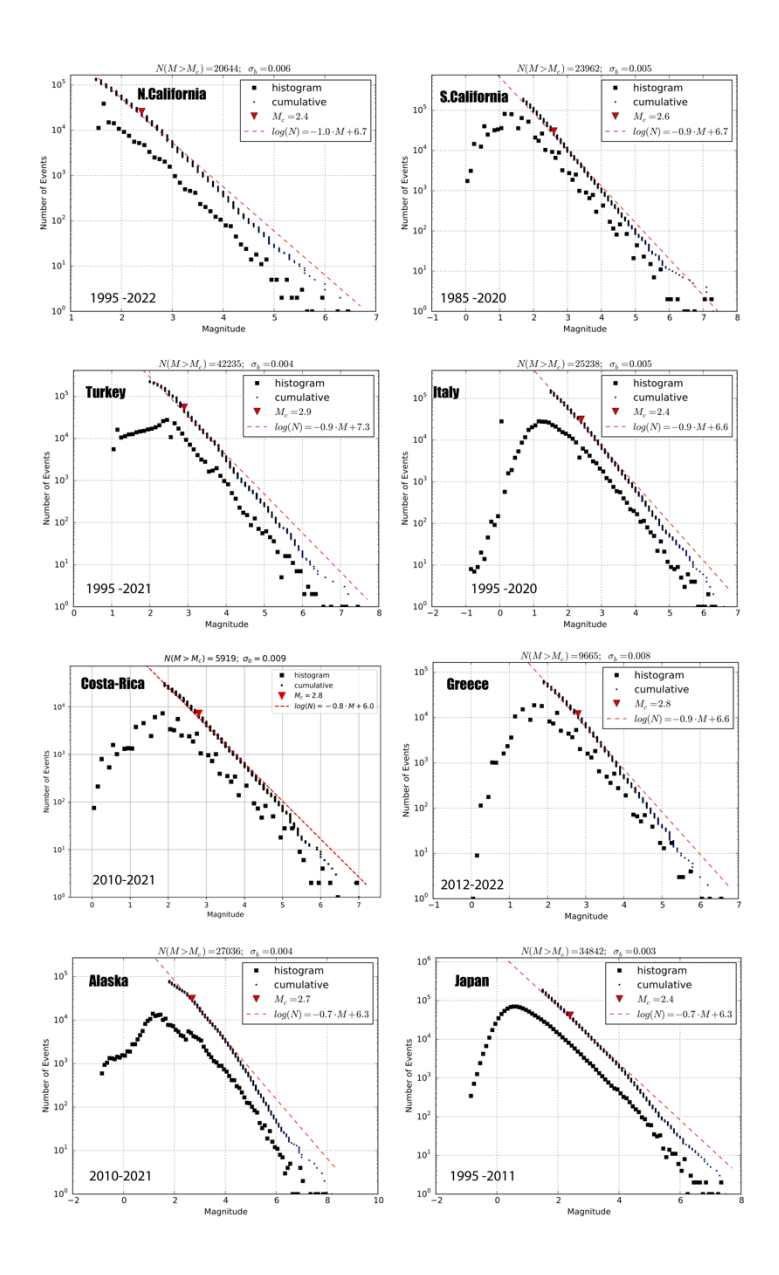


Figure S1. Magnitude distributions with regional calculated magnitude of completeness,  $M_c$ , and Gutenberg-Richter relationships determined for the eight catalogs considered in this study. The black squares give the total number of events in 0.05 to 0.2 magnitude intervals and black dots give the cumulative number of events larger than the corresponding magnitude. The inverted red triangles indicate the estimated regional magnitude of completeness, with the dashed red curve indicating the corresponding maximum likelihood estimate of the Gutenberg-Richter relationship parameters listed in the insets. The time period of each catalog considered is shown at the lower left corner of each panel.

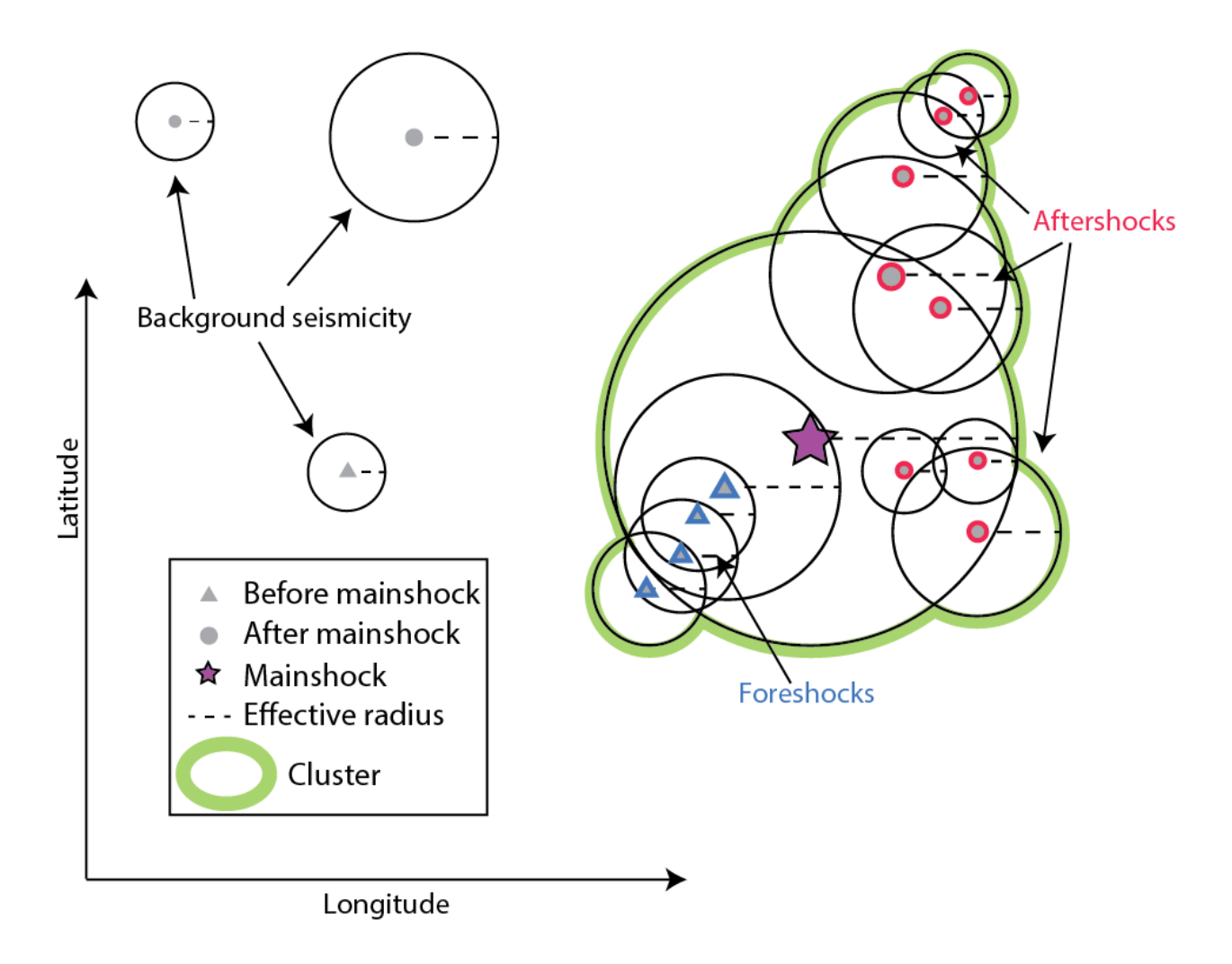


Figure S2. The Time Magnitude Clustering (*TMC*) method is illustrated by a seismicity map plot with earthquakes that occurred prior to the mainshock (triangles) or after (circles). The designated foreshocks are plotted in blue, aftershocks in red and mainshock in magenta. The circles represent the effective radius of each earthquake with the effective area of the linked cluster shown by a green thick line.

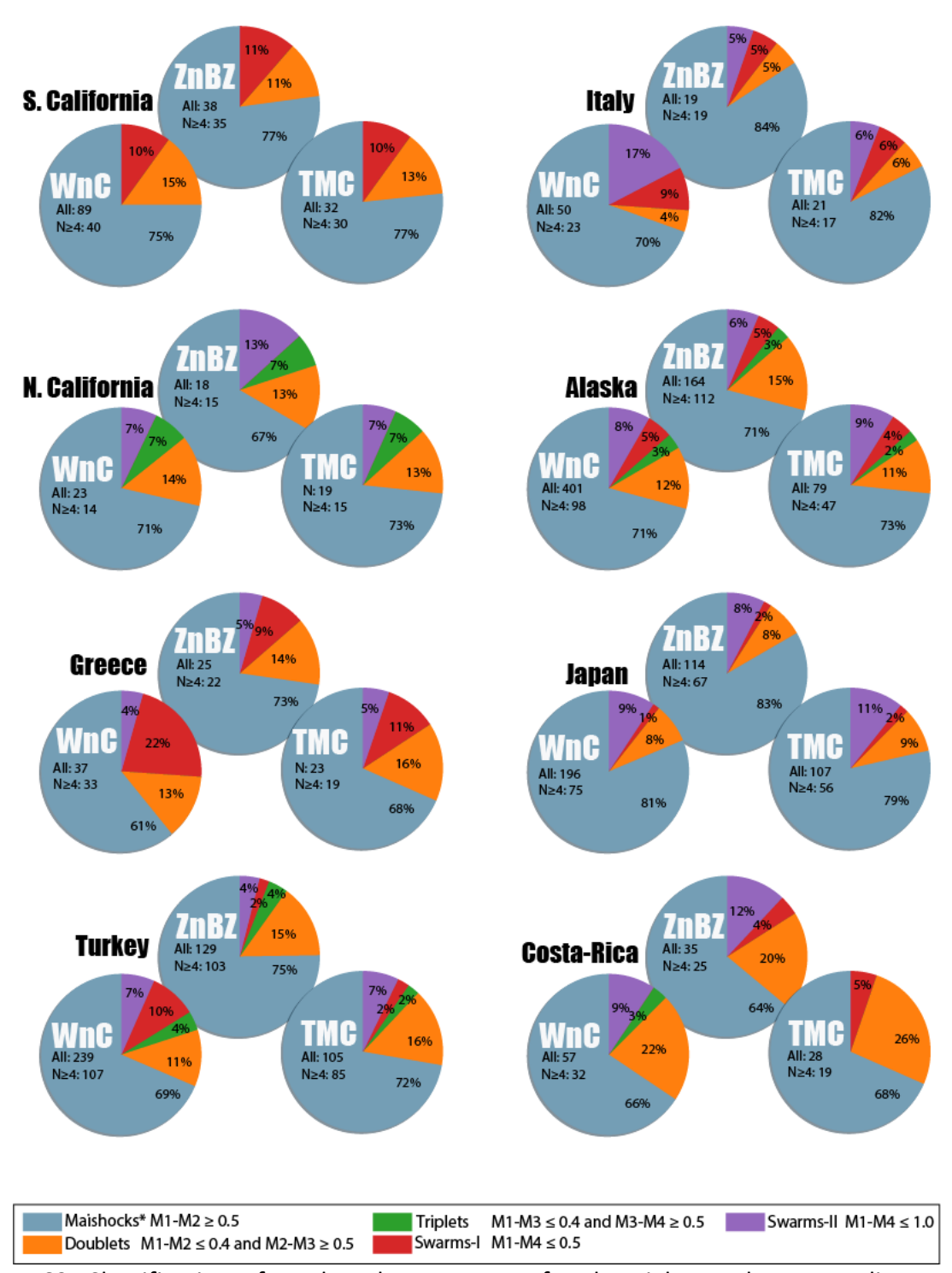


Figure S3. Classification of earthquake sequences for the eight catalogs according to the metrics for earthquake clusters defined by the WnC, ZnBZ, and TMC algorithms. The sequence classification criteria are specified in the legend. The largest earthquake in the cluster, the mainshock, is  $M_1$  and  $M_n$  is the n<sup>th</sup> largest in the magnitude-ordered sequence. Mainshocks are only considered if they have a magnitude  $\geq 2.0$  units above  $M_C = 3.0$  for each network. Swarms type 1 are sequences of  $M_1$ - $M_4 \leq 0.5$ , and swarms' type 2 are  $M_1$ - $M_4 \leq 1.0$ . The results for the eight networks are shown with the total number of examined mainshocks in each catalog as defined by the clustering algorithm plotted in each pie diagram ("All"). Sequences with a dominant mainshock ( $M_1$ - $M_2 \geq 0.5$ ) and with  $\geq 4$  associated events (foreshocks and/or aftershocks) are designated mainshock\* events.

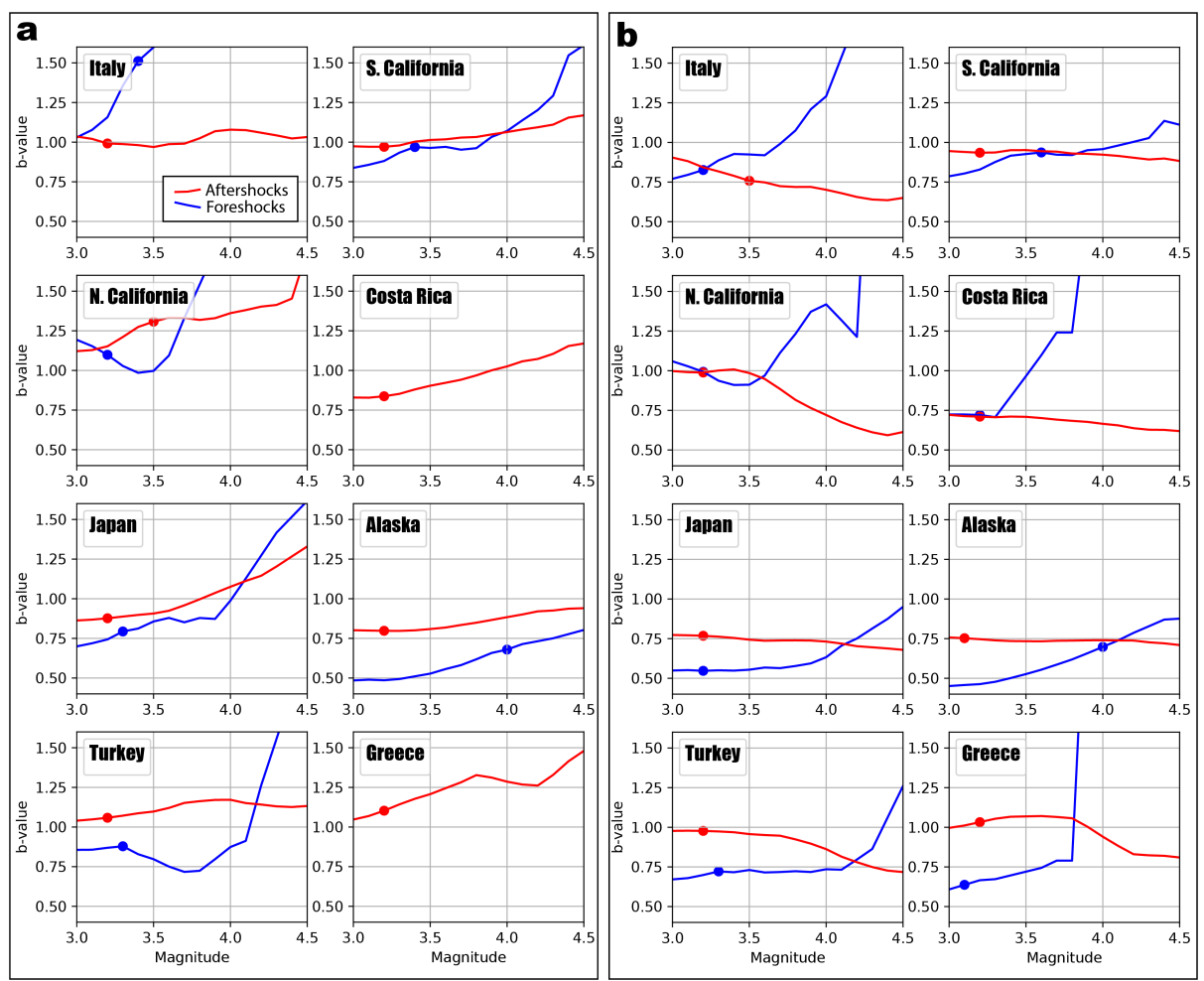


Figure S4. Variations in b-value estimates of foreshocks (blue lines) and aftershocks (red lines) as a function of the assumed  $M_C$  levels, calculated for the eight catalogs using the ZnBZ clustering method. Foreshocks and aftershock sequence are considered (a) from the strongest foreshock in the foreshock sequence to the mainshock origin time, and from the mainshock to the last aftershock, and (b) for the entire foreshock and aftershock sequences (including the mainshock). The best fit  $M_C$  levels and b-values (dots) are defined by the K-S test method (see text, and Figure 4).

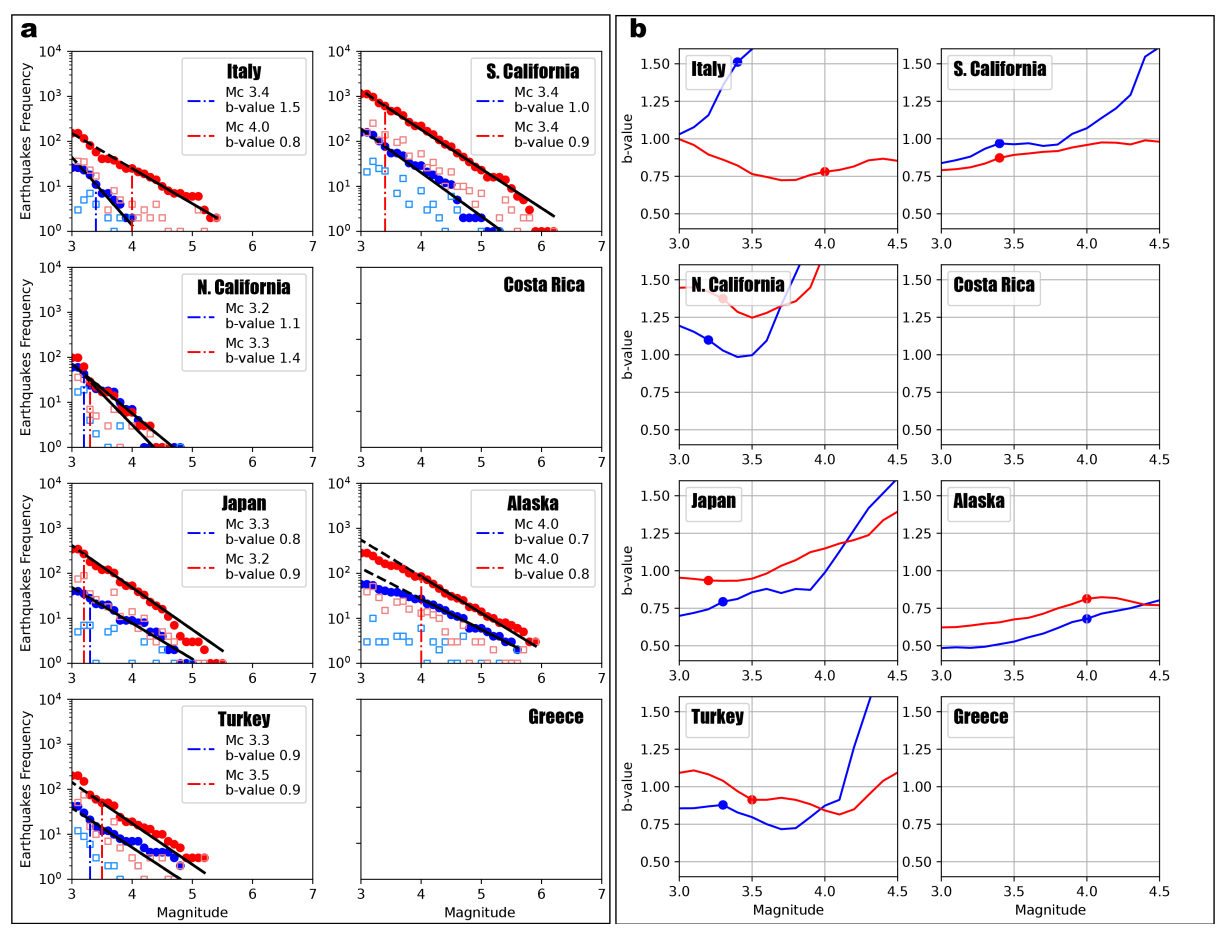


Figure S5. (a) Comparison between b-values, of composite foreshocks (blue) and aftershocks (red) sequences using the individual sequence time interval following the largest foreshock to the mainshock to constrain the length of the aftershock sequence considered in the composite distributions. (b) The variations of b-value with respect to assumed  $M_C$  level is plotted for each of the considered catalogs.

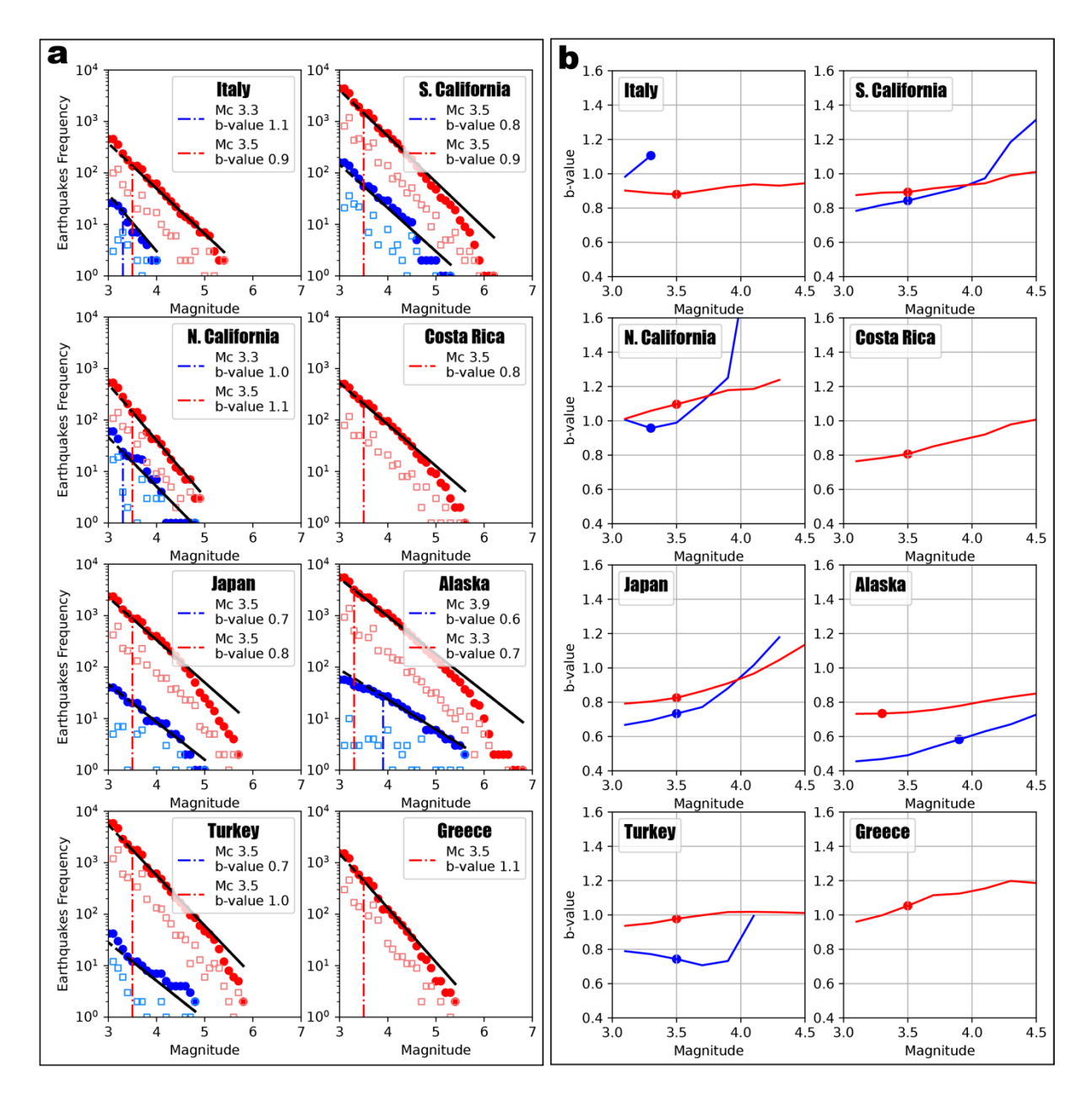


Figure S6. (a) Comparison between b-values, using dM=0.2, of composite foreshock (blue) and aftershock (red) sequences, with foreshocks selected from the largest earthquake in the foreshock sequence to the origin time of the mainshock. (b) The variations of b-value with respect to assumed  $M_c$  level is plotted for each of the considered catalogs.

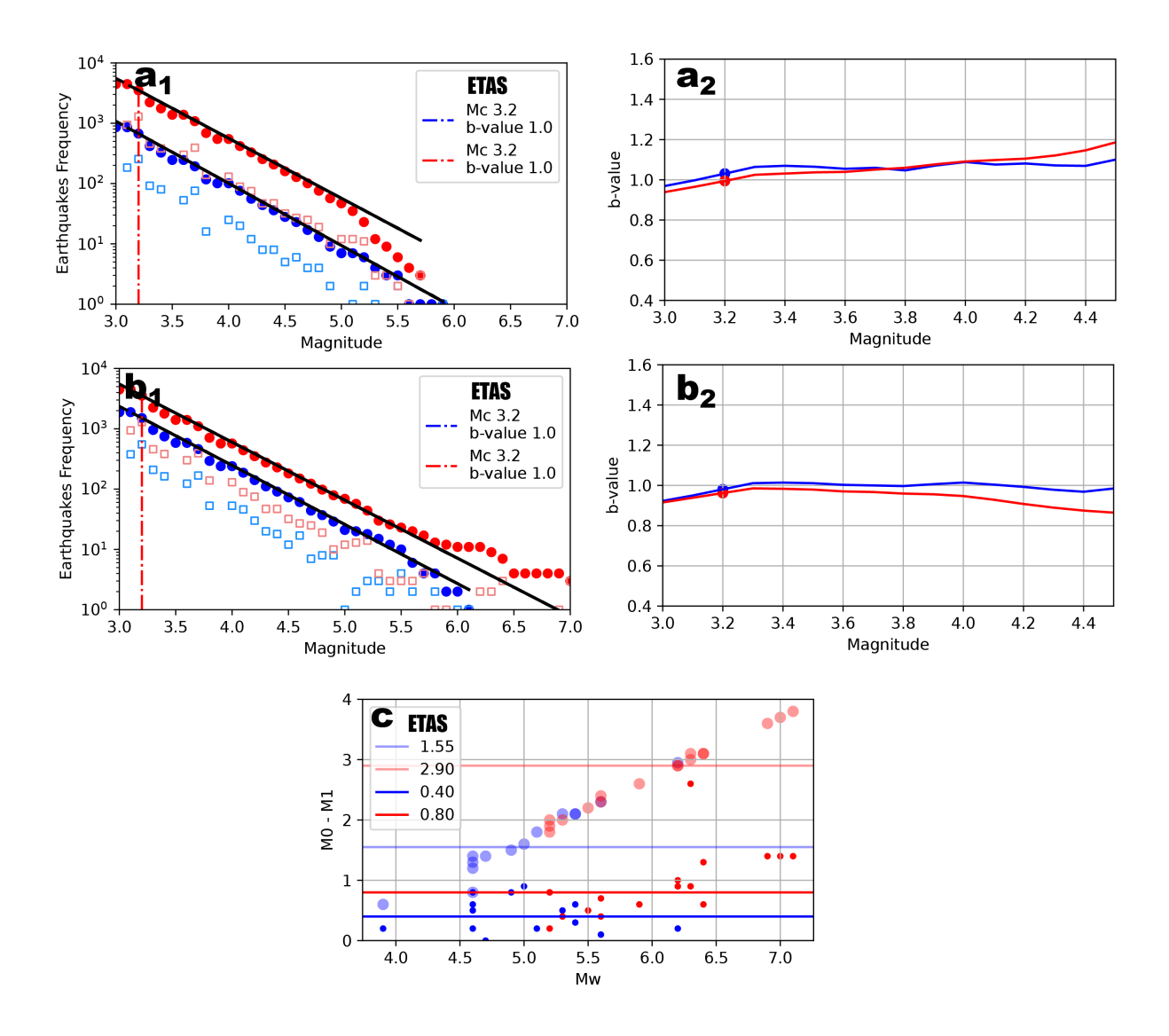


Figure S7. The b-value analysis for foreshock (blue dots) and aftershock (red dots) composite sequences in a synthetic catalog generated by an ETAS model with a simple power law decay with distance following the algorithm of Brodsky (2011) using the WnC clustering algorithm. Foreshocks are selected from the largest earthquake in the foreshock sequence to the mainshock origin time ( $a_1$ ), and for the entire foreshock sequence compared with the aftershocks combined with the mainshocks ( $b_1$ ). The variations of the b-values with respect to the considered  $M_C$  are shown for each subset at the right panels ( $a_2$  and  $b_2$ ). c) The magnitude differences between the mainshock and the largest aftershock (small solid red dots), mainshock and median of aftershocks (large pale red dots), largest foreshock and the successive largest foreshock (small solid blue dots), and largest foreshock and median of all foreshocks (large pale blue dots) is shown with respect to the mainshock or largest foreshock  $M_W$ . The median of each of the populations is shown by the horizontal lines with corresponding color coding.

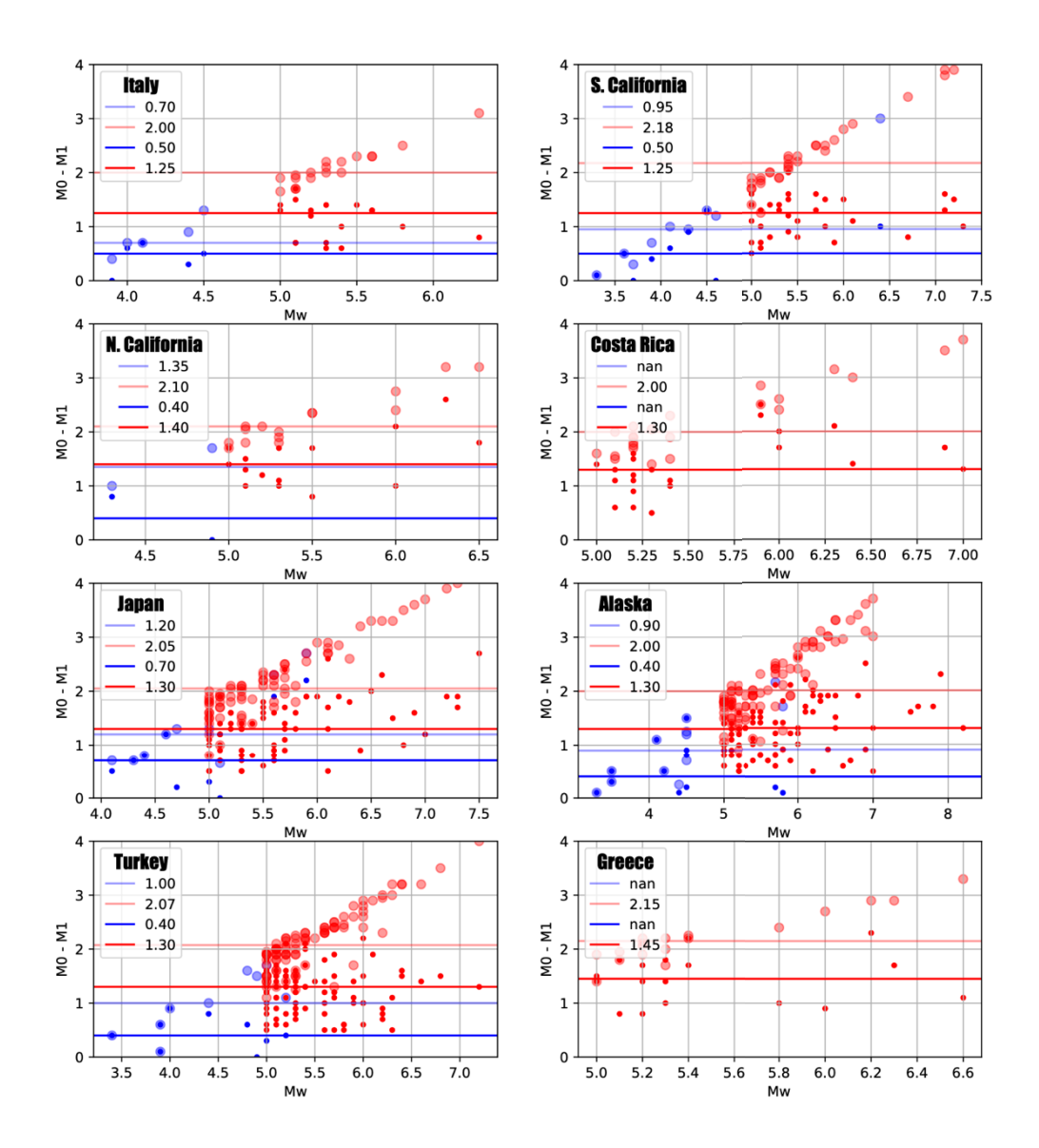


Figure S8. The magnitude differences between the mainshock and the largest aftershock (small solid red dots), mainshock and median of aftershocks (large pale red dots), largest foreshock and the successive largest foreshock (small solid blue dots), and largest foreshock and median of all foreshocks (large pale blue dots) is shown with respect to the mainshock or largest foreshock  $M_W$ . The median of each of the populations is shown by the horizontal lines with corresponding color coding.

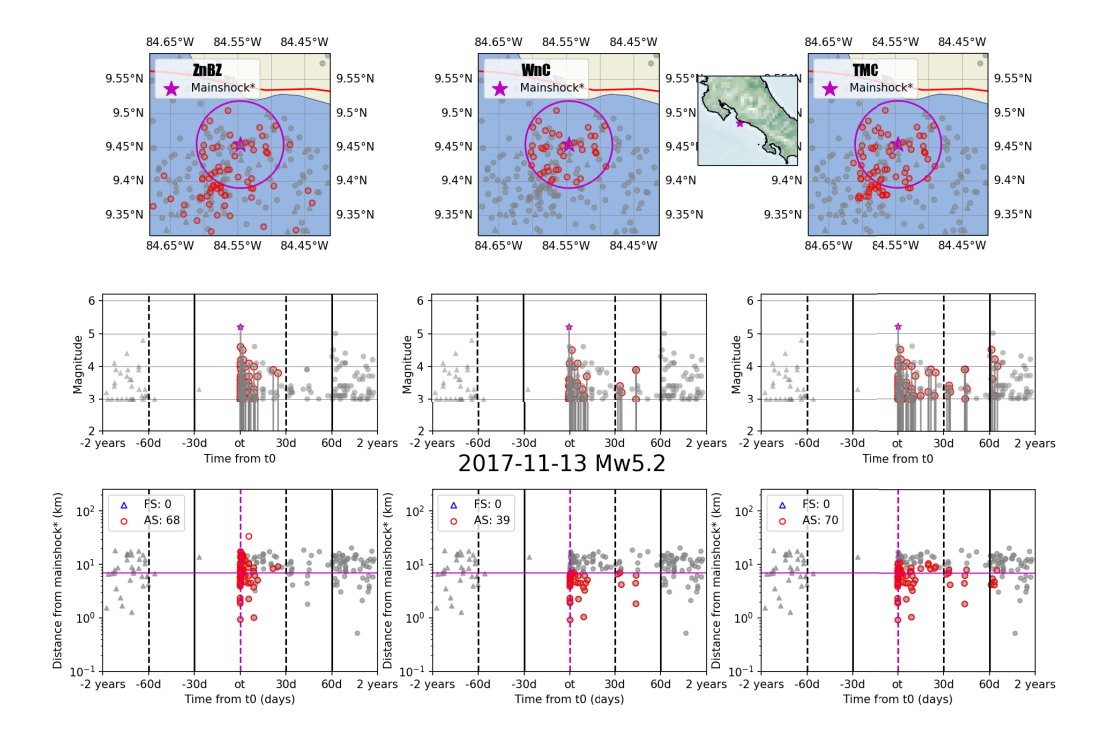


Figure S9. Comparison between ZnBC, WnC, and TMC clustering methods for the Costa Rica event on November 13, 2017 ( $M_W$  5.2). Top panels show a map view of the seismicity that occurred prior to the mainshock (triangles) and after the mainshock (circles). Gray symbols are background activity for each method. The designated foreshocks are plotted in blue and aftershocks in red. Magenta line represents the effective radius of the mainshock (see Eq. 1). Time lines are shown for the seismicity in each map as functions of magnitude (middle row) and epicentral distance from the mainshock (lower row), with the same color scheme.

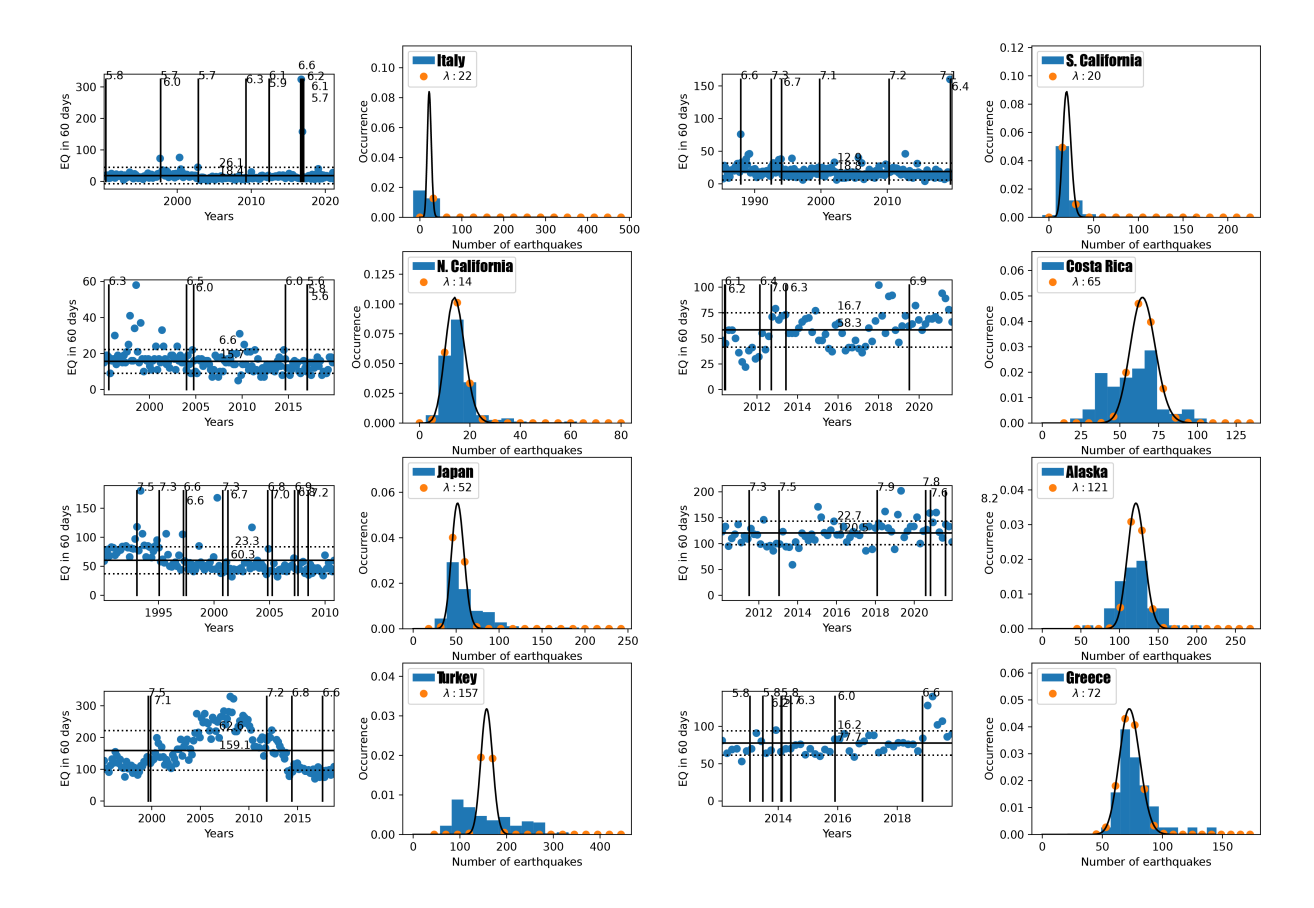


Figure S10. The background rates based on the *ZnBZ* clustering algorithm, measured by number of earthquakes per 60 days, for the tested regional catalogs are shown in the individual panels with the histograms of the measured rates. The Poissonial mean rate,  $\lambda$ , is shown on the legends of each catalog with the fitted Poissonian curve, and the estimated rates in each bin (orange dots).

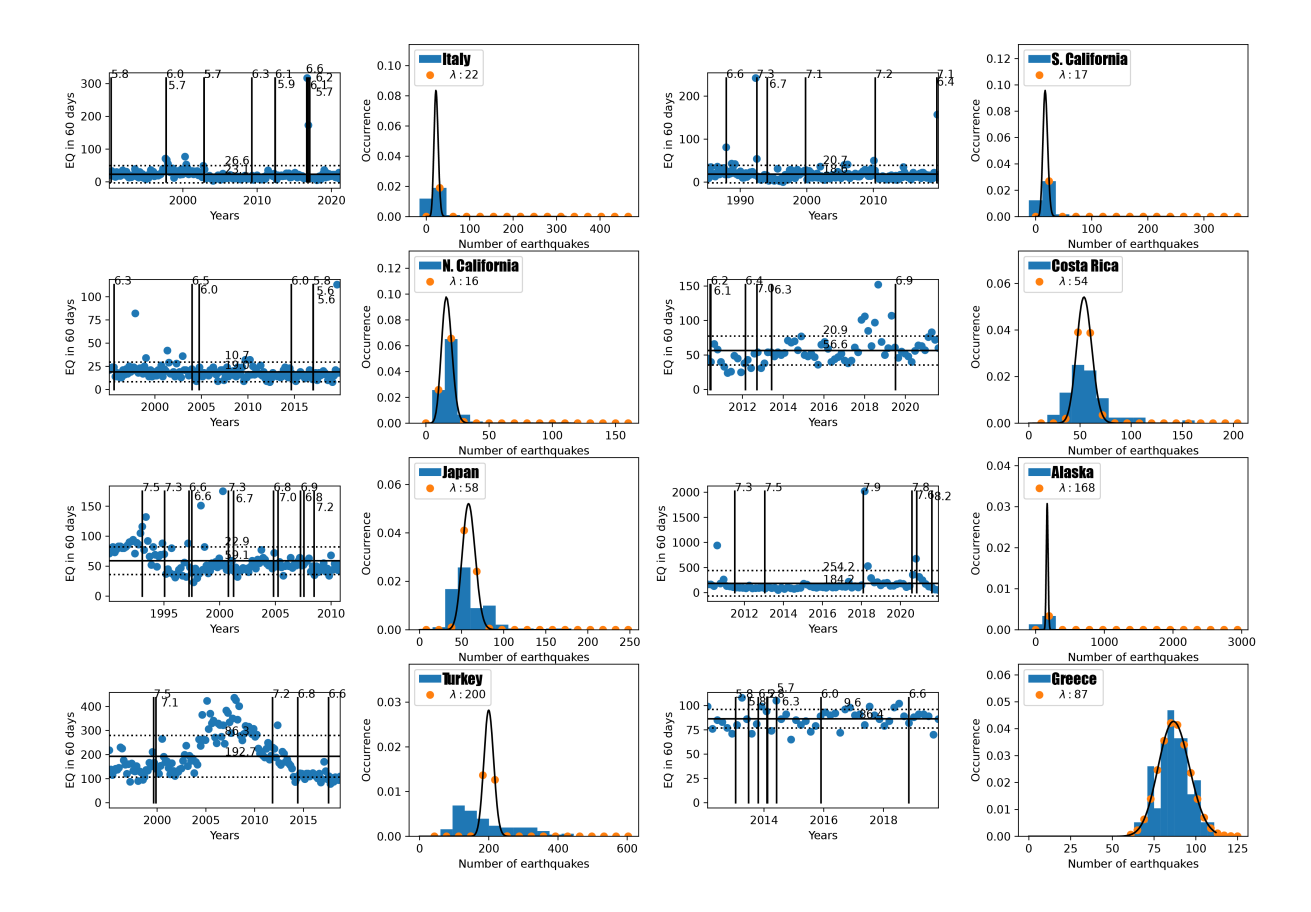


Figure S11. The background rates based on the TMC clustering algorithm, measured by number of earthquakes per 60 days, for the tested regional catalogs are shown in the individual panels with the histograms of the measured rates. The Poissonial mean rate,  $\lambda$ , is shown on the legends of each catalog with the fitted Poissonian curve, and the estimated rates in each bin (orange dots).

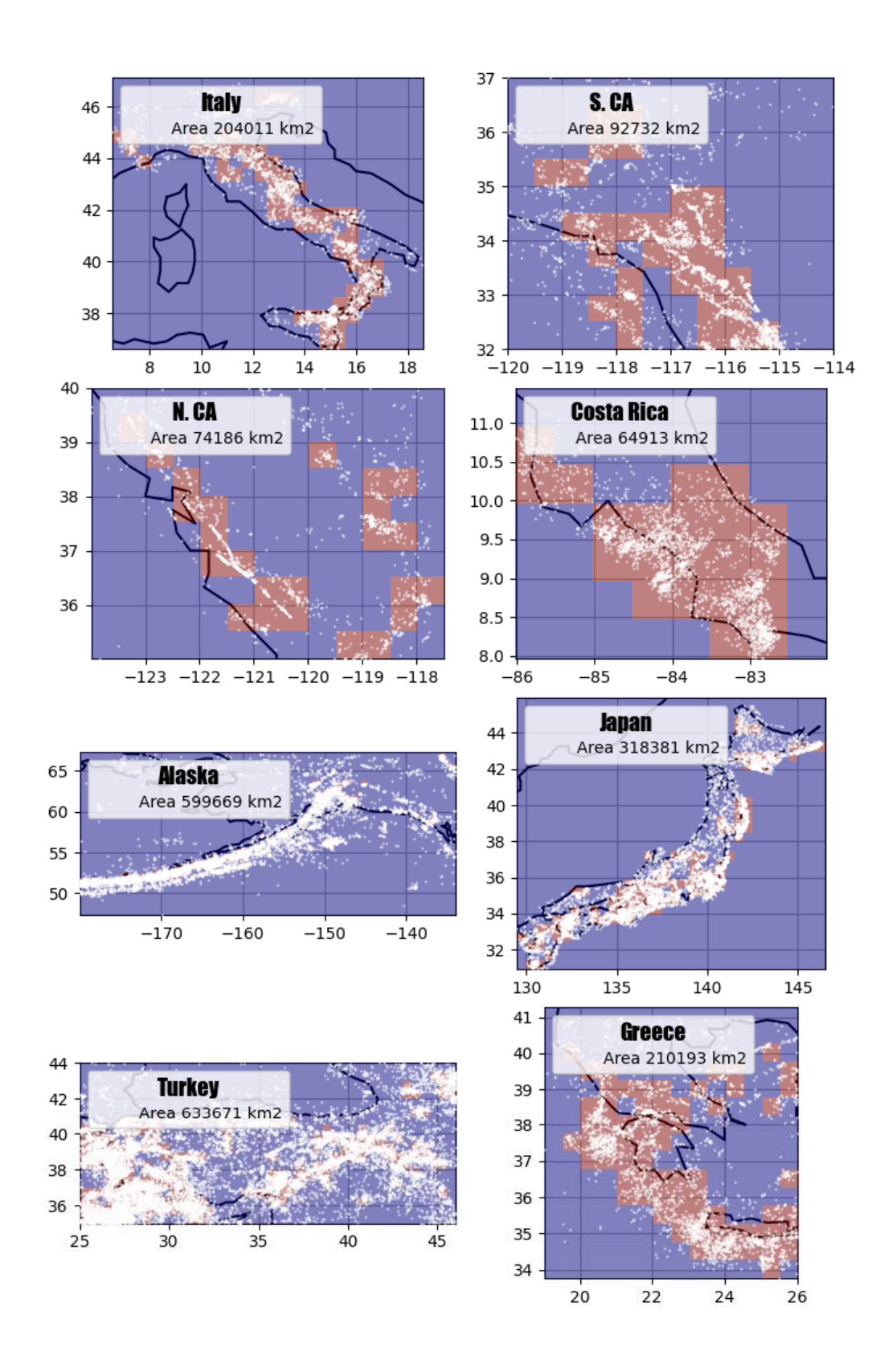


Figure S12. Seismogenic area for the ZnBZ method is estimated using a regular grid of 0.5°. The number of background earthquakes from the declustered catalog of  $M_c \ge 3.0$  is counted for each grid cell. The area is integrated for grid cells having a number of earthquakes larger than 10% of the maximum gridded seismicity (brown cells). We note that some of the brown cells are not visible due to event density (e.g., Turkey, Alaska, and Japan)

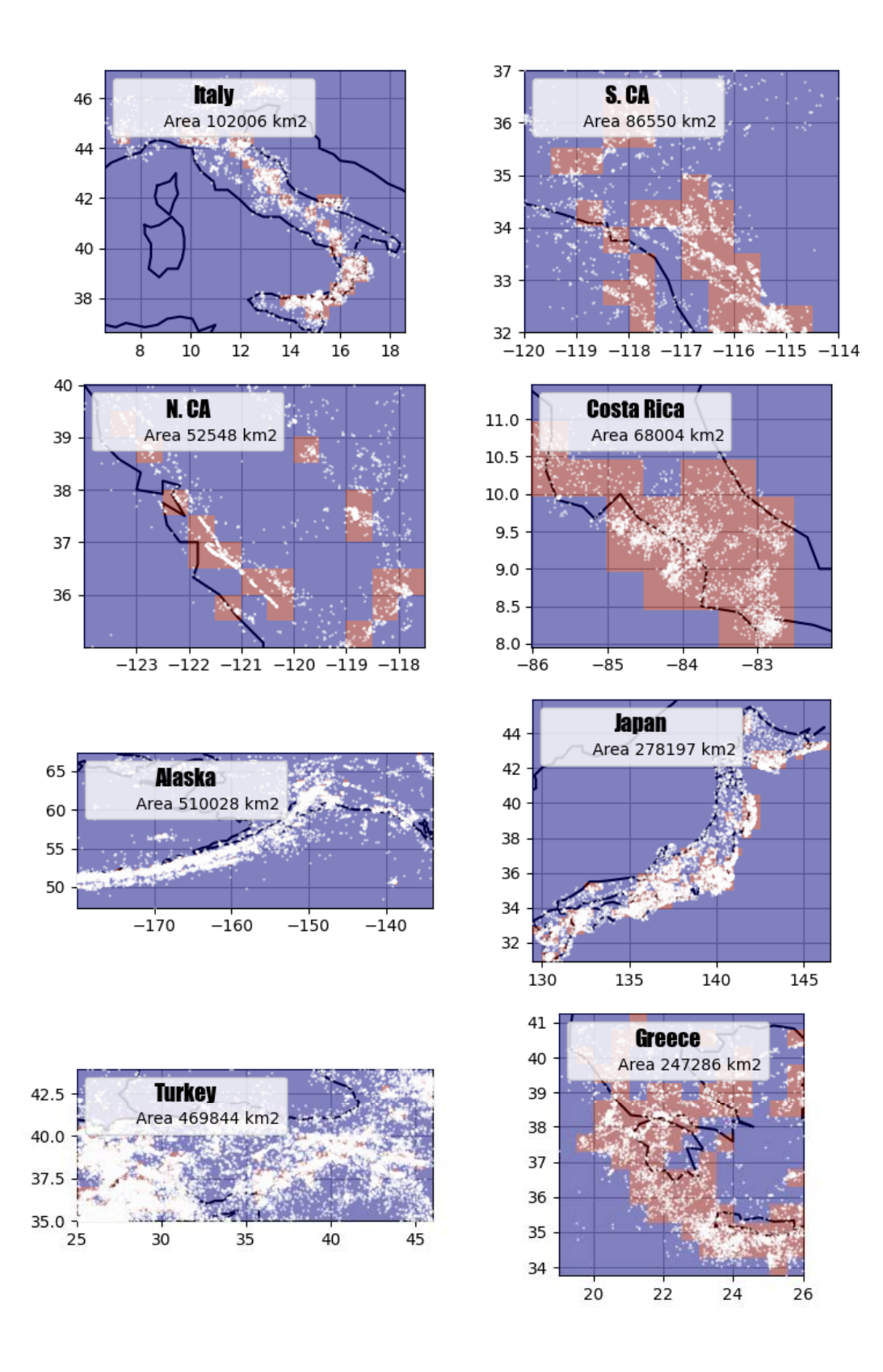


Figure S13. Seismogenic area for the TMC method is estimated using a regular grid of 0.5°. The number of background earthquakes from the declustered catalog of  $M_c \ge 3.0$  is counted for each grid cell. The area is integrated for grid cells having a number of earthquakes larger than 10% of the maximum gridded seismicity (brown cells). We note that some of the brown cells are not visible due to event density (e.g., Turkey, Alaska, and Japan).

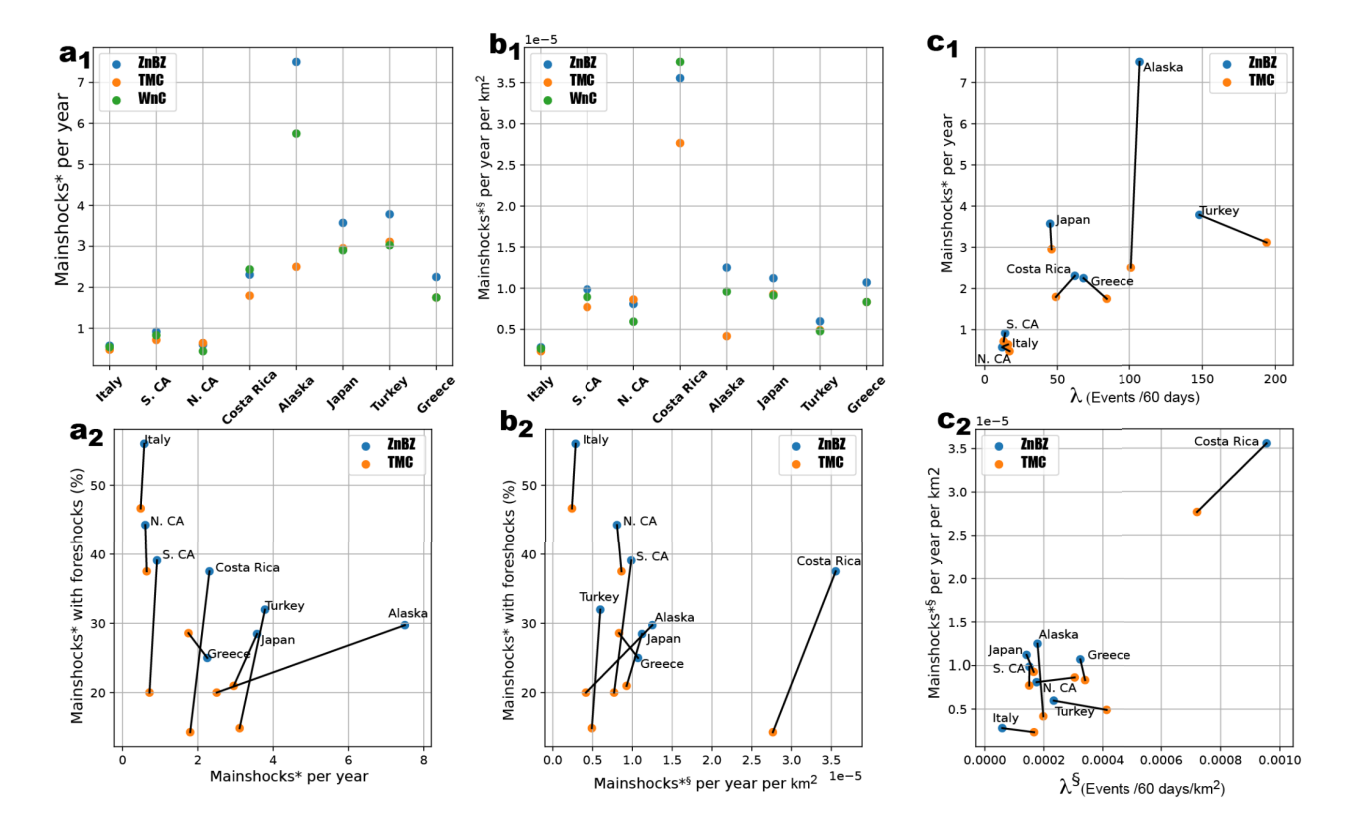


Figure S14. The mainshock\* rate (earthquakes per year) is shown in each catalog for the ZnBZ, TMC, and WnC clustering algorithms ( $a_1$ ), and then by mainshocks\* density (b1), scaled by the seismicity area of each catalog (Figs. S12, and S13). The mainshocks\* rates and mainshocks\* density rates for the ZnBZ and TMC catalogs are plotted versus the percentage of mainshocks\* with foreshocks considering only earthquakes within 2.0 magnitude units below the mainshock magnitude (Fig. 5c), for each catalog ( $a_2$ , and  $b_2$  respectively). The estimated background seismicity rate,  $\lambda$  (number of background earthquakes per 60 days), is plotted versus the mainshocks\* rate for the ZnBZ and TMC catalogs ( $c_1$ ) and the estimated background rate density,  $\lambda$ § is plotted versus the mainshock\* rate density for each catalog ( $c_2$ ).

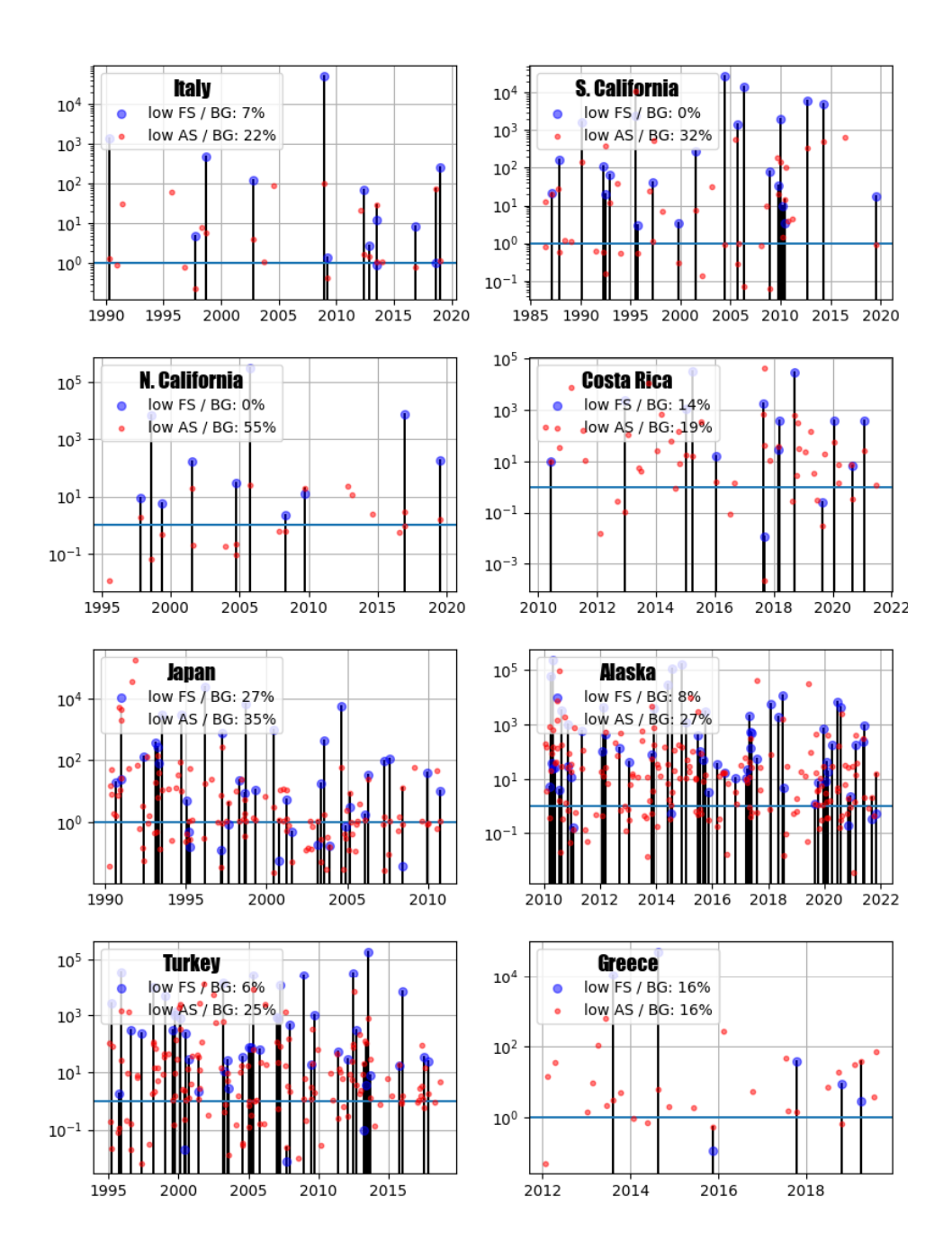


Figure S15. The ratio of foreshock rate to background rates (blue dots), and the ratio of aftershock rate to background rates (red dots) are shown for all individual sequences for the eight catalogs using the *ZnBZ* clustering method. The background, foreshock, and aftershock rates are measured in a circular area with a radius defined by the maximum epicentral distance of the cluster from the mainshock. The time windows of the background rates are calculated for each individual sequence; defined from the beginning of each catalog to the first foreshock. The time windows of the rates of the foreshock and aftershock sequences are defined by the individual durations of each sequence. The percentage of the ratios for which either the foreshock or aftershock rates are lower than the background rate are presented in the legends (blue and red, respectively).

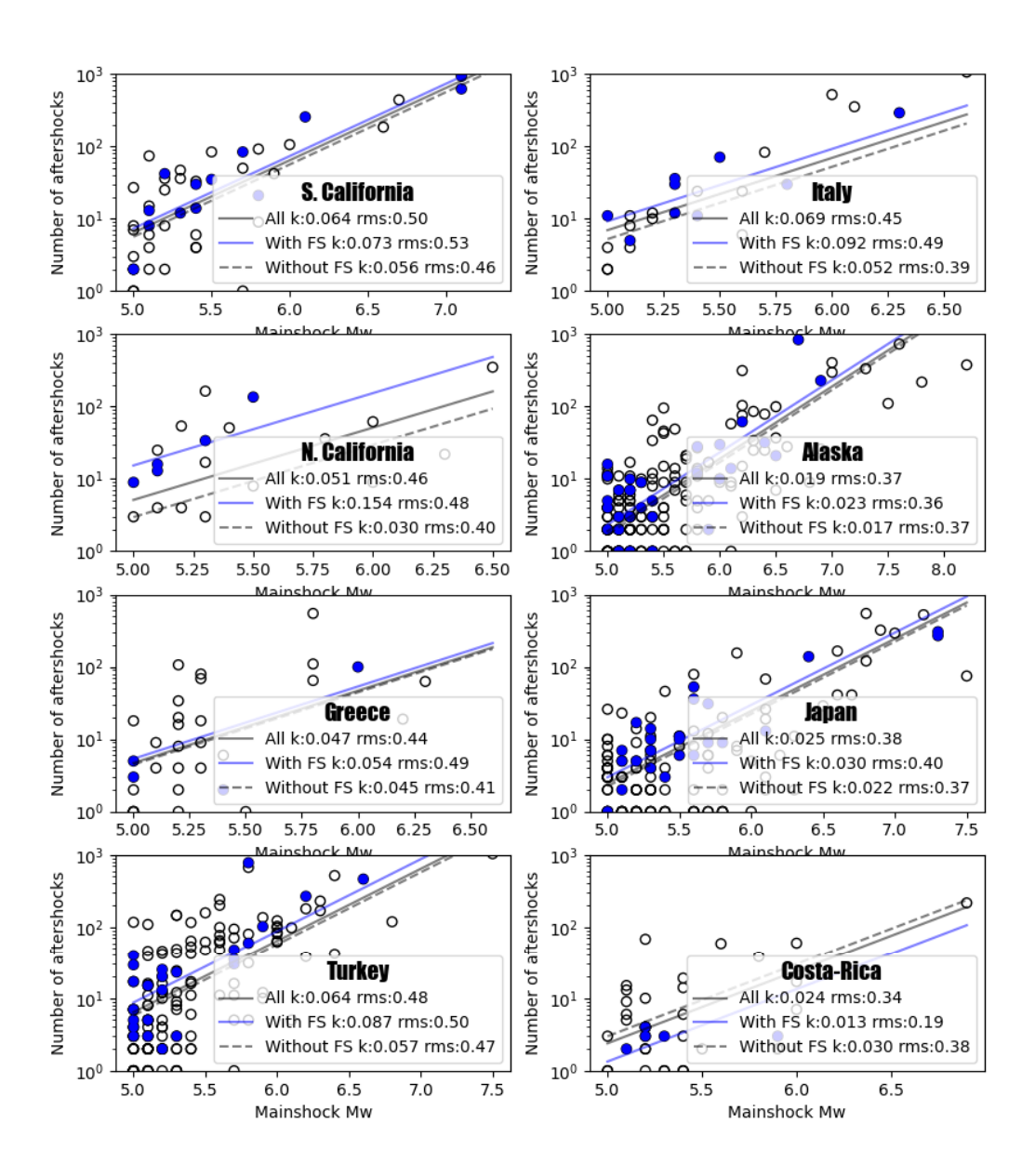


Figure S16. Aftershock productivity for mainshocks\* of *ZnBZ*, for mainshocks with foreshocks (blue filled circles) and mainshocks without foreshocks (open circles). The power law general fit, with a slope of 1, is shown by the black line and separately for the two groups, with or without foreshocks, by the blue and dashed lines, respectively.

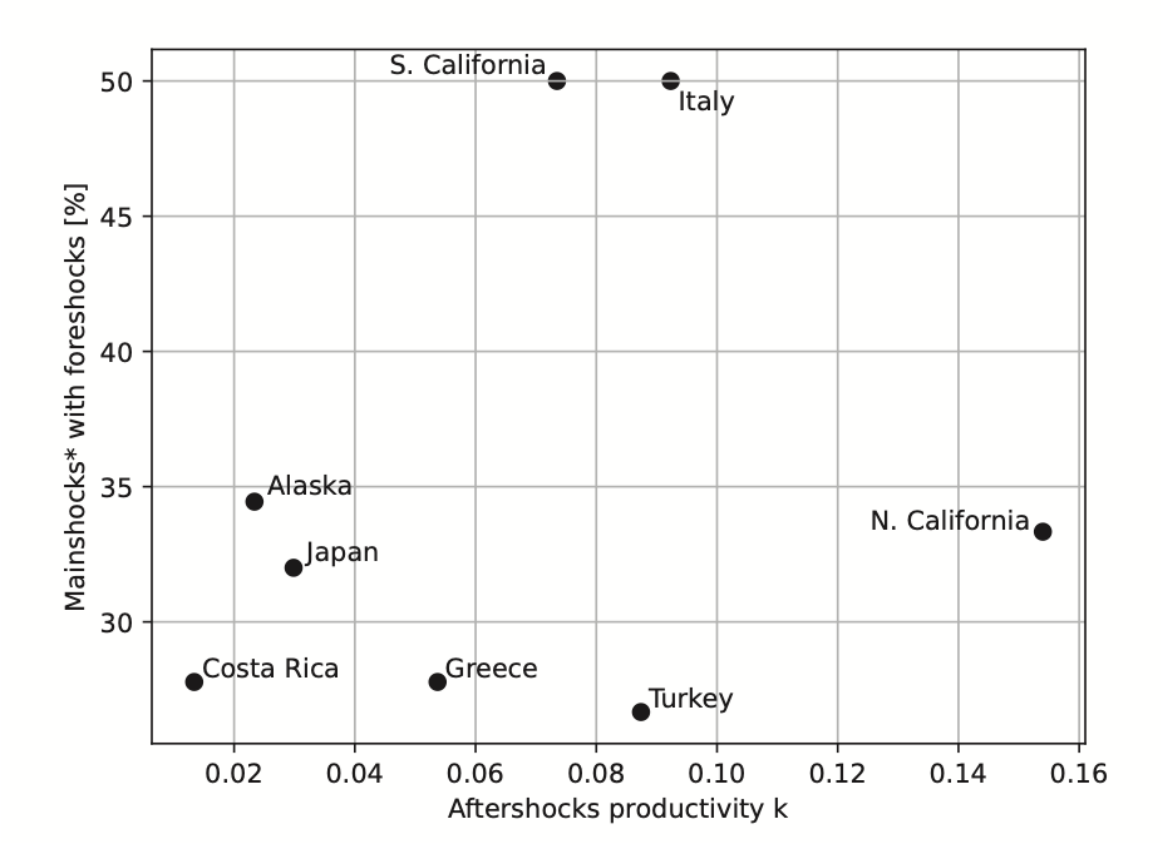


Figure S17. The relationship between the percentage of mainshocks\* with foreshocks and aftershocks productivity k. We note the lack of a coherent trend.

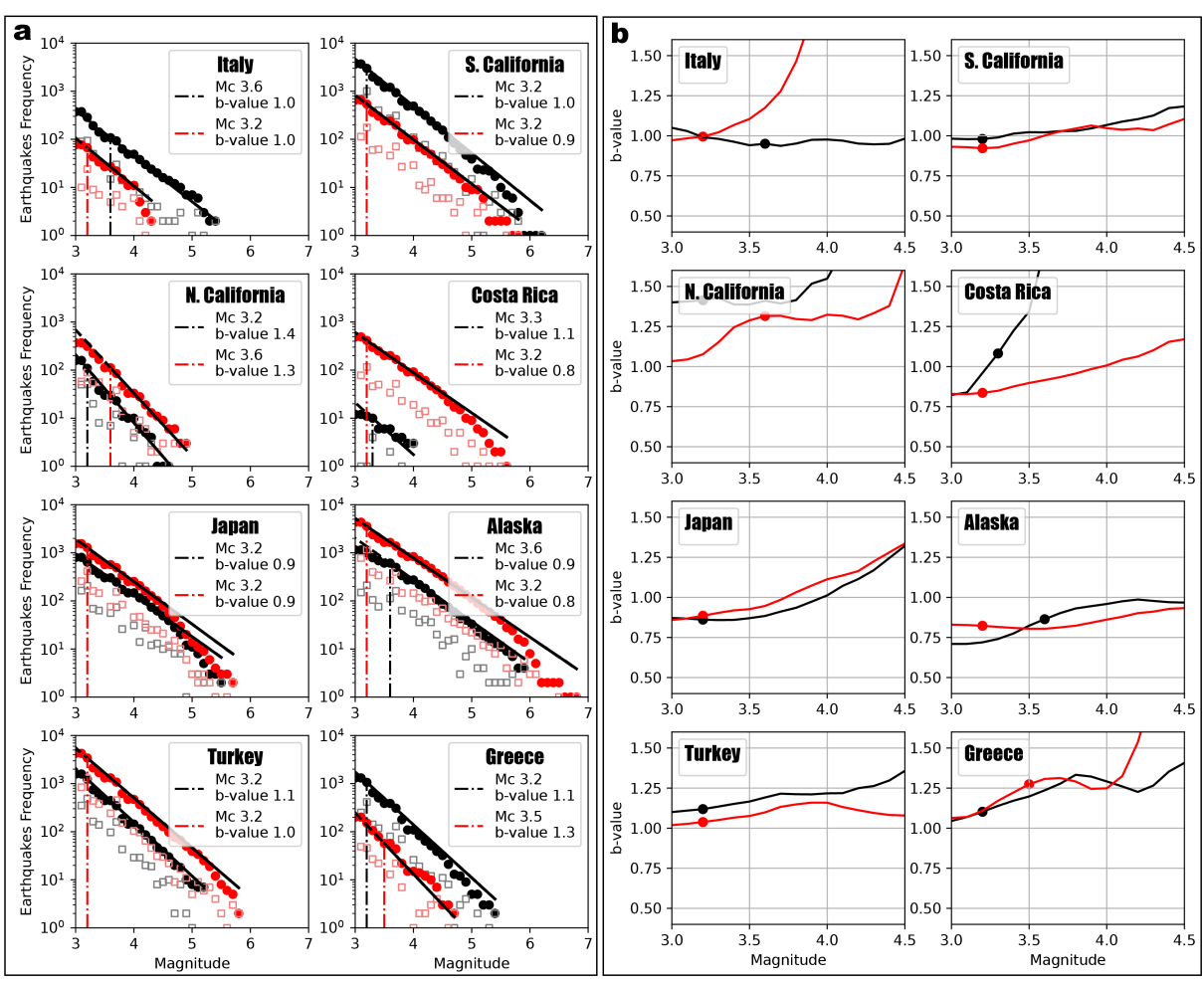


Figure S18. Comparison between b-values, of composite aftershocks of mainshocks\* with identified foreshocks (black) and without observed foreshocks (red), using the ZnBZ clustering algorithm. (b) The variations of b-value with respect to assumed  $M_C$  level is plotted for each of the considered catalogs.

#### Figure Bundle S1

Comparison between *ZnBC*, *WnC*, and *TMC* clustering methods for eight catalogs. Top panels show a map view of the seismicity that occurred prior to the mainshock (triangles) and after the mainshock (circles). Gray symbols are background activity for each method. The designated foreshocks are plotted in blue and aftershocks in red. Magenta circles represent the effective radius of the mainshock (see Eq. 1). Time lines are shown for the seismicity in each map as functions of magnitude (middle row) and epicentral distance from the mainshock (lower row), with the same color scheme.